



Electrochemical Model of Solid Oxide Fuel Cell for Simulation at the Stack Scale

I. Calibration Procedure on Experimental Data

Arata Nakajo,^{a,z} Zacharie Wullemmin,^a Patrick Metzger,^b Stefan Diethelm,^a
Günter Schiller,^c Jan Van herle,^a and Daniel Favrat^a

^aLaboratoire d'Énergétique Industrielle (LENI), Institut de Génie Mécanique, Ecole Polytechnique Fédérale de Lausanne, 1015 Lausanne, Switzerland

^bWürth Solar PV power plants division, D-74523 Schwäbisch-Hall, Germany

^cGerman Aerospace Center (DLR), Institute of Technical Thermodynamics, D-70569 Stuttgart, Germany

Lifetime prediction and improvement of solid oxide fuel cell (SOFC) devices require a reliable electrochemical model that supports the implementation of degradation phenomena. This study comprises two parts. This Part I describes the calibration of an electrochemical model based on physical principles for simulation at the stack scale. Part II presents the further implementation of degradation models. A distinction is made between the two most common cathode materials, lanthanum strontium manganite and lanthanum strontium cobalt ferrite. The experimental data used for the parameter estimations was gathered by two segmented set-ups. The calibrations enabled to reproduce adequately the measurements over a wide range of operating conditions. The optimal values of the physical parameters were inside the ranges reported in literature. Unambiguous discrimination could not be achieved between variations (i) in the choice of electrode rate-determining steps, (ii) data on the properties of the materials found in literature and (iii) empirical relations for the steam-methane reforming reaction. However, these model variations do not affect significantly the predicted magnitudes and distributions of the field variables assumed to govern the degradation processes at the SRU scale, compared with the uncertainties on the degradation phenomena to be implemented in Part II.

© 2011 The Electrochemical Society. [DOI: 10.1149/1.3596433] All rights reserved.

Manuscript submitted December 28, 2010; revised manuscript received March 29, 2011. Published July 8, 2011.

The core of any solid oxide fuel cell (SOFC) device is the membrane electrode assembly (MEA). Most of the modelling effort is focused on the description and understanding of the electrochemical processes taking place in the MEA. The level of accuracy and refinement depends on the issue to be solved. The affordable computational time is not identical for optimisation^{1,2} or simulations of the dynamic behaviour³⁻⁵ of a whole SOFC system, calculation of the temperature profile in a single repeating unit (SRU) to mitigate structural failures⁶⁻⁸ or identification of the relation between electrode performance and microstructure^{9,10}. Different phenomena, such as heat transfer or fluid dynamics, can be selectively neglected, depending on the emphasis in the study.

A major drawback of SOFCs is the degradation of their performance, even during steady-state operation, which currently exceeds the specifications for large-scale commercialisation. Identifying the causes of degradation is a subject of extensive ongoing research, which has already shed light on some phenomena, related to physico-chemical alterations of the materials and interfaces. Coarsening of the electrode microstructure results in a reduction of the effective triple-phase boundary length (TPBL), where the electrochemical processes take place¹¹⁻¹⁶. Formation of insulating phases that alter the electrochemical processes, such as lanthanum (LZO) or strontium zirconates (SZO) in cathodes based on lanthanum strontium manganites (LSM), have been observed after operation¹⁷⁻¹⁹. Similarly, impurities in the raw materials used for the manufacturing of anodes made of nickel and yttria-stabilised zirconia (Ni-YSZ) are believed to promote the formation of glassy phases at the interfaces between the constituents.²⁰ Phase transformation is a possible explanation for the decrease of ionic conductivity of YSZ during aging,^{21,22} which affects the electrolyte and ionic-conducting network in the composite electrodes. The electrode contamination does not necessarily affect button-cell tests in alumina test rigs, but can prevail in SOFC systems, where different materials and fuels are used for cost and engineering reasons. Volatile chromium species released by the metallic components of the stack or system and transported by the air can deposit and block the active sites of both LSM-YSZ and lanthanum strontium cobaltite ferrite (LSCF) cathodes, even though the underlying mechanisms and severity of the degradation differ.²³⁻²⁸

A mitigation strategy of degradation involves different research fields. It starts with the selection of materials, in the light of their absolute performance but also long-term stability. High electrochemical activity and stability are usually contradictory aims. Because the degradation processes depend among others on temperature, overpotential and gas composition, button-cell and short stack endurance tests highlight a very strong dependence of the degradation on the operating conditions.^{11,29,30} This results in different but interrelated local degradation rates in a SOFC stack.³¹ The control strategy^{3,32} and stack and system design³³ are therefore vital to extend the lifetime of SOFC devices in the view of the lowest cost of electricity delivered to the end-user.

An electrochemical model for the mitigation of the degradation at the SRU/stack scale must provide the reliable prediction of the performance of the cells, within a large range of operating conditions. Micro-scale models have been developed to investigate the elementary processes of the oxygen reduction reaction (ORR) or hydrogen oxidation (HO).³⁴⁻³⁸ They have then been used to design electrodes and current collection^{9,39} with the support of percolation theories to provide the correct effective conductivities and TPBL in the composite structures.^{40,41} The current trend consists in using the discrete element method to handle changes in composition or microstructure at the particle size,¹⁰ or in using a combination of imaging techniques to record the actual geometry of an electrode or interface, and modelling techniques such as the lattice Boltzmann method.^{42,43} Despite the availability of an analytical solution in some micro-modelling cases,^{34,44} the link between micro- and SRU/stack modelling in general has remained loose for a long time. Many electrochemical models for the simulation of the behaviour of SOFC SRUs and stacks use semi-empirical relations, because of the advantage in terms of ease of implementation and computational time.⁴⁵⁻⁵¹ They can reproduce experimental current-voltage (IV) characteristics within the typical range of operating conditions of SOFC stacks but they fail when it comes to the calculation of local quantities within the electrodes, such as local overpotential or compositions in multi-component gas mixtures. This strongly limits their relevance for degradation-oriented investigations. A recent change coincides with the introduction of elementary heterogeneous chemical kinetics in the SOFC field.⁵²⁻⁵⁷ At the same time, standards in levels of detail have been determined for a satisfactory description of some phenomena. The simulation of diffusion

^z E-mail: arata.nakajo@epfl.ch

processes in a thick anode support requires the dusty-gas model (DGM).^{58,59} However, such modelling frameworks currently focus on a representative channel along the flow path^{60–62} and are seldomly found in design-oriented SRU models^{63,64} and not yet combined with structural analysis.

Even the most refined modelling approaches embed fitting parameters with however a physical meaning to reproduce not only qualitatively but also quantitatively the response of a SOFC. Parameter estimation and design of experiment tools^{65,66} are of great value for model calibration, as a direct measurement of each parameter is unthinkable. Using such procedures as well as dynamic simulations place a requirement on computational time. Implementation of a calibrated electrochemical model in thermo-electrochemical and structural SRU models can allow a quick, reliable and inexpensive evaluation of technological solutions, such as the type of cell, particularly the type of electrode, or the sealing or GDL system, depending on the target application. The risks of failure ensued from typical situations a SOFC stack may face during service can be evaluated, and the procedures adjusted. The insertion of degradation phenomena in the electrochemical model further allows lifetime predictions, and hence the needed safety margin for a given specification.

A major difficulty in the application of such tools is to efficiently gather experimental data. Automated segmented-cell setups⁶⁷ have several benefits for this task. One can take advantage of their ability to provide insights into local quantities for different but linked purposes.^{68,69} Investigations can focus either on the dependence of the cell behaviour on the operating conditions or on the spatial distribution and interaction between the phenomena. A large amount of information can be effectively gathered by a few experimental runs, as the composition of the gases and the temperature vary along the flow path, depending on the rate of the chemical and electrochemical reactions. This ability helps to mitigate imprecision due to degradation, when a large amount of experiments have to be performed one after the other. Design of experiment tools can optimise the arrangement of the segments and operating conditions to detect or alternatively avoid large spatial gradients.

The context of this study is the prediction and mitigation of ends-of-service induced either by an exceedingly severe degradation of the stack performance after long-term operation, or by discrete structural failures due to the combined effects of aging and operating procedures. The focus is on intermediate temperature, anode-supported SOFC. The electrochemical and degradation models for simulations at the SRU/stack scale developed here are presented in two parts. Part I focuses on the calibration of a one-dimensional electrochemical model. The implementation and study of degradation phenomena is described in Part II,⁷⁰ together with a more detailed model of the cell and interconnection, to identify the limitations of the one-dimensional simplification. A short literature survey on the current understanding of SOFC degradation and electrochemistry is presented to provide guidance in the choice of modelling approaches. In an effort to retrieve knowledge from existing modelling studies at the micro-scale for consistent further implementation of degradation processes, specific approaches are used for LSM-YSZ and LSCF cathodes. In the latter case, the approach of Adler et al.³⁴ and Svensson et al.^{35,71} is adapted and tested for simulation at the SRU scale. The electrochemical model is calibrated on data gathered by two segmented-cell setups.^{67,68,72} The effect of the choice of rate-determining step (RDS) and of the materials properties data from the literature is discussed in the light of accuracy for the prediction of the cell performance and further implementation of the selected degradation phenomena in Part II, i.e. consistency in the prediction of relative contributions to the polarisation losses.

Modelling Approach

Field equations.—The main zones in a SRU, e.g. manifold and electrochemically-active area, are spatially discretised along the gas-flow direction, and they include the local one-dimensional electro-

chemical model. The modular units, implemented in gPROMS,⁶⁶ an equation-oriented process modelling tool, can be assembled in both gas flow and stacking directions, the former being sufficient to analyse experimental data from a segmented SRU. The one-dimensional nature of the models enables fast calculations but restricts their application to either co- or counter-flow configurations, with a fairly uniform gas distribution in the SRU. The calculation of the gas velocity is based on plug-flow simplification. It does not account for the detailed geometry of the interconnection system. It therefore represents better a GDL/interconnection made of a cellular solid or the SOFCConnex concept,⁷³ than the case of milled channels in a metallic interconnect (MIC). The generic shape of a modular element is depicted in Fig. 1a. Possible connection boundaries are Γ_1/Γ_8 and $\partial\mathcal{R}_1$. The species on the fuel side are restricted to H_2 , H_2O , CO , CO_2 , CH_4 and N_2 .

The model is not fully dynamic in terms of species transport and heat transfer, since only thermal inertia of the solid components and gases are accounted for. The energy conservation of the cell, Eq. 2 and of both top and bottom MICs, Eq. 1 provides the temperature profile in the solid structure T_s . Their terms are detailed further below in Eq. 3 to Eq. 10

$$\lambda_s \frac{\partial^2 T_s}{\partial y^2} + \dot{Q}_{s,cond} + \dot{Q}_{s,conv} + \dot{Q}_{s,ht} + \dot{Q}_{s,bc} = \rho_s c_{hs} \frac{\partial T_s}{\partial t} \text{ in } \mathcal{R}_1, \mathcal{R}_7 \quad [1]$$

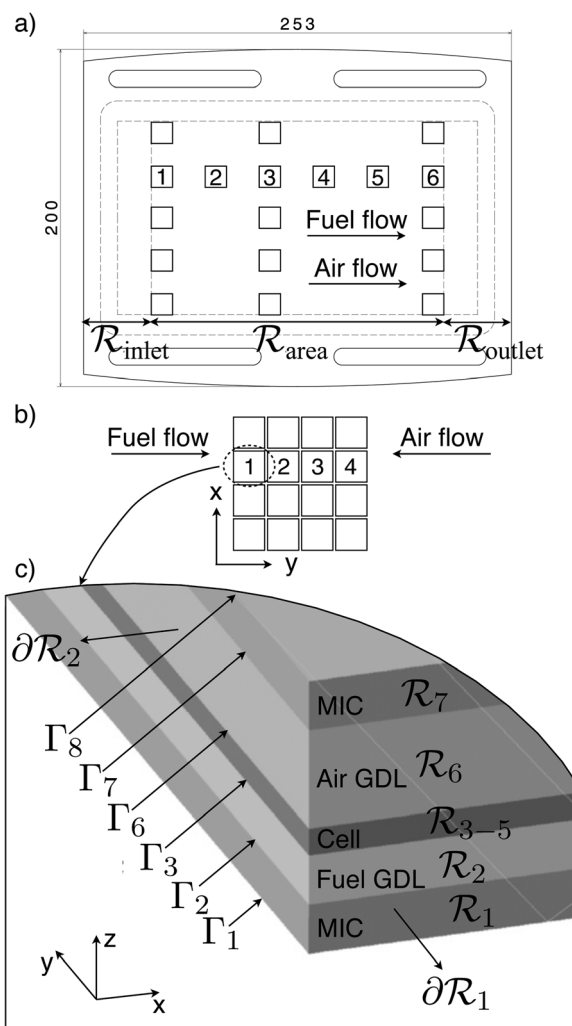


Figure 1. (a) Description of the domains and boundaries in the 1D model. The cell layers are merged in \mathcal{R}_{3-5} , which is detailed in Fig. 2. (b) In-plane arrangement of the segments in the DLR setup and (c) view of the Flame-SOFC SRU design, along with the location of the segments in the LENI-EPFL setup.

$$\lambda_s \frac{\partial^2 T_s}{\partial y^2} + \dot{Q}_{srx} + \dot{Q}_{scond} + \dot{Q}_{sconv} = \rho_s c_p h_s \frac{\partial T_s}{\partial t} \text{ in } \mathcal{R}_{3-5} \quad [2]$$

The approach is identical for all domains. The terms for the rate of volumetric energy change \dot{Q}_s differ for the MICs (\mathcal{R}_1 and \mathcal{R}_7) and the MEA (\mathcal{R}_{3-5}), because of the chemical and electrochemical reactions and heat transfer with the surroundings.

The cell layers are discretised in the electrochemical model, but merged in \mathcal{R}_{3-5} in the field equations. Similarly, the thermal inertia of the GDLs and sealants are embedded in the MICs, but their in-plane thermal conductivities are neglected. \dot{Q}_{srx} is used to relocate in the cell the rate of volumetric thermal energy generated by the chemical and electrochemical reactions. The energy released by the chemical reactions is computed from the balance of species at the anode-gas interface, assuming that all methane and carbon monoxide fluxes towards the anode are globally consumed by the steam-methane reforming (SMR) and the water-gas shift (WS) reactions

$$\begin{aligned} \dot{Q}_{srx} = & \frac{N_{CH_4}|_{GDL-an}}{h_s} (-dH_{OSMR} - dH_{OWS}) + \frac{N_{CO}|_{GDL-an}}{h_s} (-dH_{OWS}) \\ & + \frac{j_{tot}}{2Fh_s} (-dH_{elchem}) - \frac{V_{SRU} \cdot j_u}{h_s} \end{aligned} \text{ in } \mathcal{R}_{3-5} \quad [3]$$

The expression implicitly contains the Joule term. Resistive losses in the MIC itself are small and not relocated. Those in the MIC oxide scale are attributed in the cell.

Computational fluid dynamic models from our group applied to similar conditions as investigated here have shown only limited temperature gradients in the z-direction in a SRU.^{68,74} A simplified approach is used here. Heat transfer by conduction through the solid structure in the z-direction is not accounted for in Eqs. 1 and 2. Conduction through the GDLs is approximated as a rate of volumetric energy change \dot{Q}_{scond} in the solid control volumes \mathcal{R}_1 , \mathcal{R}_{3-5} and \mathcal{R}_7

$$\dot{Q}_{scond} = \frac{\lambda_g}{h_s h_{3-5}} (T_{3-5} - T_s) \text{ in } \mathcal{R}_1, \mathcal{R}_7 \quad [4]$$

$$\dot{Q}_{scond} = \frac{\lambda_2}{h_2 h_s} (T_1 - T_s) + \frac{\lambda_6}{h_6 h_s} (T_7 - T_s) \text{ in } \mathcal{R}_{3-5} \quad [5]$$

Convection heat transfer between the gases and the solid structure is embedded in \dot{Q}_{sconv} . Common relations are used for the computation of heat transfer coefficients h_g^c (Ref. 75)

$$\dot{Q}_{sconv} = \frac{h_g^c}{h_s} (T_g - T_s) \text{ in } \mathcal{R}_1, \mathcal{R}_7 \quad [6]$$

$$\dot{Q}_{sconv} = \sum_g \frac{h_g^c}{h_s} (T_g - T_s) \text{ in } \mathcal{R}_{3-5} \quad [7]$$

\dot{Q}_{shl} and \dot{Q}_{shc} refer to boundaries $\partial\mathcal{R}_2$ and Γ_1 and Γ_8 (see Figs. 1 and 2). \dot{Q}_{shl} corresponds to the rate of volumetric energy change due to averaged radiation exchange between the sides of the SRU and its surroundings. Heat exchange by radiation between the SRU and its surrounding is modelled in a simplified manner, i.e. each node is coupled to an equivalent front node of the insulation. The exchange with above and underneath, and front and rear nodes is neglected⁷⁶

$$\dot{Q}_{shl} = \frac{C_{shl}}{L_x} \varepsilon \zeta (T_{savg}^4 - T_{isl}^4) \text{ in } \mathcal{R}_1, \mathcal{R}_7 \quad [8]$$

$C_{shl} = (h_{MIC} + h_{GDL} + h_{3-5}/2)/h_{MIC}$ is a geometrical correction factor for the GDL and sealant heights, which do not directly interact with the insulation or furnace. \dot{Q}_{shc} varies depending on the assembly of the modules. It includes thermal exchanges by either radiation with the surroundings or thermal conduction with above and underneath SRUs. The former case refers to top/bottom SRUs

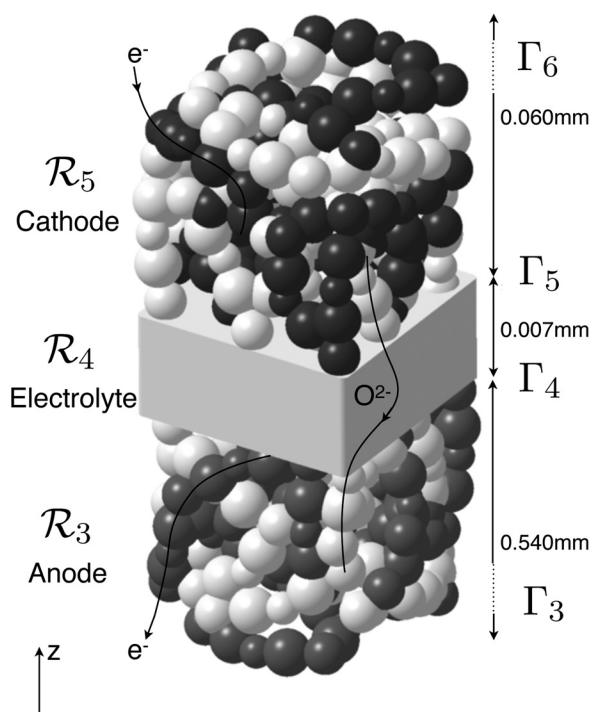


Figure 2. Representation of the MEA of a SOFC, along with the denomination of the domains and interfaces. Case of LSM-YSZ cathode.

in a stack or a separately-tested SRU, while the latter is applied to SRUs in a stack.

$$\dot{Q}_{shc} = \frac{C_{bc}}{L_x} \varepsilon \zeta (T_s^4 - T_{isl}^4) \text{ in } \mathcal{R}_1, \mathcal{R}_7, \text{ isolated SRU} \quad [9]$$

$$\dot{Q}_{shc} = \frac{2}{h_s^2} \lambda_s (T_{shc} - T_s) \text{ in } \mathcal{R}_1, \mathcal{R}_7, \text{ stacked SRU} \quad [10]$$

$C_{bc} = (A_{isl} + A_{SRU})/A_{SRU1D}$ is a geometrical correction factor corresponding to additional heat losses over sealing or manifold areas not explicitly considered due to the 1D assumption. Adiabatic conditions for a SRU in a stack yield $\dot{Q}_{shc} = 0$. The energy conservation on the insulation is

$$\varepsilon \zeta (T_{savg}^4 - T_{isl}^4) = \frac{\lambda_{isl}}{h_{isl}} (T_{isl} - T_{amb}) \quad [11]$$

$T_{isl} = T_{fnce}$ is enforced, depending on the conditions of the experiment.

The conservation of energy of gases, Eq. 12, as well as the conservation of species, Eqs. 13 and 14 considers variations of gas densities ρ_g for a consistent handling of internal steam-methane reforming (\mathfrak{R}_{SMR}^m). The ideal gas assumption is used and the required properties are computed from Todd et al.⁷⁷

$$\frac{\partial(\rho_g u_g H_g)}{\partial y} + \dot{Q}_{gconv} + \dot{Q}_{grx} = \rho_g c_p h_g \frac{\partial T_g}{\partial t} \text{ in } \mathcal{R}_2, \mathcal{R}_6 \quad [12]$$

$$\frac{\partial(\rho_g u_g \omega_i)}{\partial y} = \frac{M_i N_i |_{GDL-an}}{h_g} \text{ in } \mathcal{R}_2, \mathcal{R}_6 \quad [13]$$

$$\frac{\partial(\rho_g u_g)}{\partial y} = \sum \mathfrak{R}_i^m \text{ in } \mathcal{R}_2, \mathcal{R}_6 \quad [14]$$

Because of the first left hand side term of Eq. 12, the rate of heat generated by the electrochemical and chemical reactions that take place in the cell rather than in the gas channels must be removed

from \mathcal{R}_2 and \mathcal{R}_6 and recast in \mathcal{R}_{3-5} using $\dot{Q}_{g,cs}$, which mirrors the first three right hand terms of Eq. 3.

Electrochemical model.—The one-dimensional electrochemical model is developed for the implementation of selected degradation phenomena in Part II (Ref. 70): (i) the decrease of ionic conductivity of 8YSZ, (ii) MIC corrosion, (iii) anode nickel particle growth, (iv) chromium contamination and (v) formation of insulating phases in the cathode. Controversy remains in the current understanding of SOFC degradation. However, the dependence of the processes on (i) local overpotentials, vacancy concentration and current density, (ii) anode and cathode gas compositions and (iii) temperature is acknowledged. The electrochemical model must therefore reliably predict the distribution of these. The influence of the TPBL in the electrodes, and of the rate-determining steps on the electrochemical performance is further needed to assess the detrimental effect of physico-chemical alterations.

The decrease of ionic conductivity of 8YSZ and the coarsening of nickel particles tend to plateaus, after an initial variation.^{78–81} In the case of nickel particle coarsening, this is due to the structural constraint enforced by the YSZ backbone. Under such assumptions, these phenomena do not provoke alone the end of life of a SOFC stack. Their quantitative prediction enables to set a safety margin to fulfil requirements over long periods and to identify alterations of the temperature distribution and ensuing thermo-mechanical stresses. In contrast, chromium contamination or development of insulating phases on the cathode side can fully block the active sites and so lead to the end of life of a stack. Therefore, computational time is spared to afford a composite model for the cathode rather than for the anode. The one-dimensional electrochemical model considers both ohmic and non-ohmic losses. The calculation of the losses in the electrolyte, the anode and the cathode terms is described later. Part II (Ref. 70) presents the modelling approach and parameters for the ohmic losses in the MICs. A small electronic conductivity of the electrolyte, which induces a slight leakage current, is included in the electrolyte.² Ohmic losses due to current constrictions in the GDLs are evaluated using analytical relations.⁸²

The electrochemical model is based on the equivalent circuit approach, which is depicted in Fig. 3. The calculation of the Nernst potential from interfacial gas composition, is based on hydrogen only, as equilibrium of the water-gas-shift reaction is approximated in the anode support. The equivalent circuit simplification, the absence of composite electrode model on the anode side and the one-dimensional description are tested for degradation prediction against a more detailed model in Part II (Ref. 70) based on the

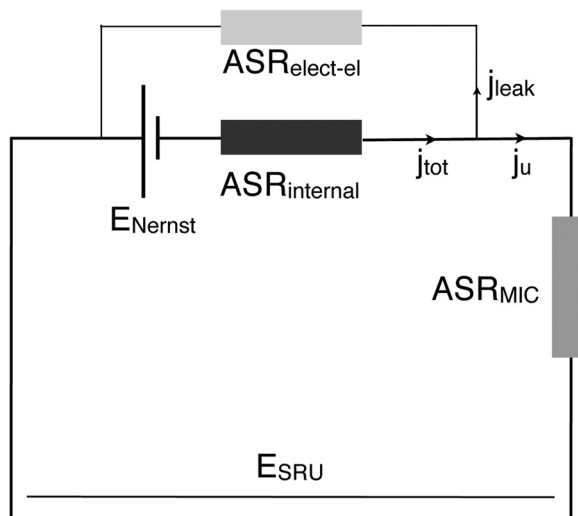


Figure 3. Equivalent circuit of the one-dimensional electrochemical model.

computation of the potential in the ionic- and electronic-conducting networks in the MEA and interconnection/GDL system.

Electrolyte and compatibility layer.—Ohmic losses in the 8YSZ electrolyte- and gadolinia (GDC) and yttria (YDC) doped ceria compatibility layer needed in the case of LSCF cathode are computed using simple relations, without differentiation of the contributions of the grain boundaries and the bulk. Thin electrolytes used in anode-supported cells have a higher resistance than thick ones relative to their thickness. The difference is significant for the typical electrolyte thickness in anode-supported cells, ranging from 4 to 10 μm . Fleig et al.⁸³ have attributed this increase in resistance to current constriction, due to the uneven interface between the dense electrolyte and the porous electrodes. Their interpolated relation satisfactorily reproduces their finite-element calculations and is used in the present work

$$ASR_{ion_{elect}} = \frac{h_{elect} - h_{cl}}{\sigma_{ion_{elect}}^e} + \frac{l_g}{\sigma_{ion_{elect}}^e} \left(\frac{l_g/d_g - 1}{d_g/l_g + 1} \right) + \frac{1 - n_{cl}}{1 + 0.5n_{cl}} \frac{h_{cl}}{\sigma_{ion_{cl}}^e}, \text{ in } \mathcal{R}_4 \quad [15]$$

In the absence of a compatibility layer, h_{cl} is set equal to zero. It should however be stressed that in reality, constriction effects depend on reaction pathways and the extension of the active zone, hence on the type of cathode and anode. Charge transfer at the interface between the YSZ electrolyte and GDC compatibility layer is neglected. The ionic conductivity of 8YSZ, GDC or YDC σ_{ion}^e strongly depends on temperature, according to

$$\sigma_{ion}^e = \frac{k_{o_{ion}}}{T_s} \exp \left[-\frac{E_{a_{ion}}}{R} \left(\frac{1}{T_s} \right) \right] \quad [16]$$

This relation is used as well for the electronic and ionic conductivity of other SOFC and SRU materials.

Anode.—Nickel volatilisation and particle coarsening depend on temperature and anode-gas composition. They detrimentally reduce the anode TPBL during operation.^{12–16} An effect on the rate determining step of the hydrogen oxidation cannot be excluded. Investigations on the hydrogen oxidation reaction in Ni-YSZ anodes are based on the observation of the response during either DC polarisation, galvanostatic current interruption (GCI) or electrochemical impedance spectroscopy (EIS). Experimental studies have first inferred possible RDS from the visible influences on the polarisation resistance of variations of hydrogen and steam partial pressure, temperature, overpotential and even electrode microstructure. Possible RDS candidates include, among others, dissociative adsorption of hydrogen, formation of hydroxyl, desorption of water, surface diffusion of species or charge transfer reaction by different spillover mechanisms. Either bulk or surface pathways can, to some extent, contribute concurrently and competitively.

Pattern anodes have been preferred for fundamental studies, since the features of their geometry are easier to control and characterise than that of composite Ni-YSZ anodes. The results highlight a linear dependence of the polarisation resistance on the TPBL, a weak dependence on the hydrogen partial pressure and a so-called catalytic effect of steam.^{84–86} The range of investigated operating conditions covers that of intermediate temperature SOFCs. Reported Tafel slopes range from 1 (Refs. 85 and 87) to 3/2,⁸⁶ and the number of arcs in the analysis of EIS measurements from 1 (Ref. 85) to 3,⁸⁸ leading to discrepancies in the interpretation of the results. The process responsible for the main arc is either an adsorption or a diffusion process on Ni (Ref. 85) or charge-transfer.⁸⁶ Bieberle et al.⁸⁴ have discarded diffusion and adsorption/desorption of water, but considered charge-transfer, removal of O^{2-} and adsorption of hydrogen as possible candidates.

The extension of the active zone in a porous Ni-YSZ anode improves the performance but complicates the understanding of the mechanisms. Conclusions drawn from experiments on pattern anodes may not hold for technological ones. The extension is expected to be around 10 μm .^{89,90} Rate-limiting electrochemical processes produce one arc in general, two in several cases, the others being attributed to gas conversion or diffusion in the stagnant gas layer over the electrode.^{89,91} Jiang et al.^{92,93} have proposed relations for SRU performance simulations from GCI and EIS measurements on Ni-3YSZ anodes. Holtappels et al.^{94,95} have tested Ni-8YSZ anodes over a wide temperature range (998–1223 K), which has highlighted a transition around 1118 K and an apparent anodic charge-transfer coefficient of 0.7. They suggest that hydrogen oxidation is controlled by charge-transfer at low temperature, while adsorption together with chemical reaction between adsorbed species seems to contribute noticeably at high temperature. The impurities may explain the strong influence of the anode response on the raw material and manufacturing route.^{20,96} In general, reported apparent reaction order on hydrogen and steam, and activation energy range from –0.5 to 1.0, 0.3 to 1.0 and 70 to 170 kJ mol^{-1} , respectively.

Modelling studies have been carried out to assist the interpretation of experimental data, primarily from pattern anodes. They highlighted the need for reliable thermodynamic data and complex dependences between the different assumed elementary steps, one being able to mimic the effect of another.^{87,97} Zhu et al.⁹⁸ have proposed a simplified elementary kinetic scheme, with a limited number of steps and a single RDS that yields an expression in Butler-Volmer form, with apparent reaction orders and charge-transfer coefficients. They favoured as RDS charge-transfer by hydrogen spillover to hydroxyl site on YSZ, which results in compatible apparent charge transfer coefficients with the data from De Boer et al.⁸⁶ Bessler et al.⁵³ have pointed out the effect of equilibrium potential on the so-called catalytic effect of steam on the electrochemical oxidation of hydrogen. Comparisons of trends produced by different single limiting charge transfer mechanisms against experimental data generally suggest hydrogen spillover is the RDS. Further investigations by Vogler et al.⁸⁷ have shown that a combination of hydrogen spillover from Ni surface to oxygen ions and hydroxyl ions on YSZ provide the best fit to experimental data. The one-dimensional spatial discretisation has suggested large surface coverage gradients on YSZ, over a large distance of 0.1 μm , compared with the particle size in technological composite anodes. The RDS was detected through a sensitivity analysis, which has revealed among all considered elementary steps four possible co-limiting RDS: (i) hydrogen spillover to YSZ, (ii) water association on YSZ, (iii) water dissociation on YSZ and, (iv) surface diffusion of hydroxyl ions adsorbed on YSZ.

SOFC stack operation under internal steam-methane reforming exhibits advantages for thermal management and system cost reasons. In such conditions, carbon monoxide can be electrochemically converted and adsorbed species on Ni can be involved in either reforming reactions or hydrogen oxidation, which therefore occur concurrently and competitively. The elementary kinetic approach formally enables a consistent handling of the situation, at the cost of difficult model implementation, large yet reliable database, and ideally the need of a discretisation of the TPB. Yet, possibly dominant effects of impurities would be neglected. To our knowledge, full coupling has not yet been performed in a SOFC model. Fast SRU models for dynamic simulation can currently not afford this level of detail. A common approach that is acknowledged of reasonable accuracy in performance modelling consists in first neglecting the contribution of carbon monoxide oxidation, and second in completely uncoupling the reforming and hydrogen oxidation reactions. It is adapted here to include in a simplified manner knowledge on (i) the dependence of electrochemical performance on TPBL and (ii) on the hydrogen oxidation, since the current knowledge does not provide a solid background for the handling of degradation in the view of altered sequences of elementary mechanisms and RDS.

Modelling of electrochemical processes on the anode side.— The correct dependence of the electrochemical model on the local conditions in a SRU is paramount for structural analysis based on the temperature profile. The coarsest practical approach to implement a correct dependence of the electrochemical model on the local conditions in the SRU consists in estimating apparent reaction orders (r_{an}^{ct}) and charge-transfer coefficients ($\alpha_{an}^a, \alpha_{an}^c$) directly from experimental data, without any assumption on the mechanisms or RDS.^{92,93} The generic expression that relates the current density j_{tot} and the overpotential η_{an}^{ct} embeds all electrochemical processes at the anode/electrolyte interface

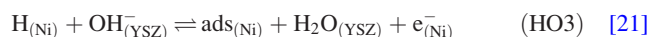
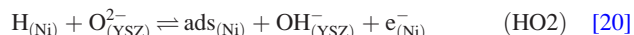
$$j_{tot} = \xi_{TPB_{an}} \cdot i_{o_{an}}^{ct} \cdot x_{H_2}^{r_{an1}^{ct}} \cdot x_{H_2O}^{r_{an2}^{ct}} \cdot \left[\exp\left(\alpha_{an}^a \frac{F}{RT_s} \eta_{an}^{ct}\right) - \exp\left(-\alpha_{an}^c \frac{F}{RT_s} \eta_{an}^{ct}\right) \right] \text{ over } \Gamma_4 \quad [17]$$

The gas molar fractions x_i at the interface are computed from the dusty-gas model. $\xi_{TPB_{an}}$ is a factor anticipating further implementation of degradation phenomena as described in Part II.⁷⁰ In the limiting case of a thick electrode, it does not depend linearly on the TPBL, but varies as the square root of the TPBL, i.e. $\xi_{TPB_{an}} = (ATPB_{an}/ATPB_{anc})^{0.5}$, as pointed out by Costamagna et al.⁴⁴ Results of the present study show a good agreement with this case. The exchange current $i_{o_{an}}^{ct}$ depends on temperature

$$i_{o_{an}}^{ct} = T_s \cdot k_{o_{an}}^{ct} \cdot \exp\left[-\frac{E_{o_{an}}^{ct}}{R} \left(\frac{1}{T_s} - \frac{1}{T_{ref}}\right)\right] \quad [18]$$

The reference temperature T_{ref} improves the quality of parameter estimations by reducing the correlation between the pre-exponential factor and activation energy.⁹⁹

Individual measurements or physical consideration are useful to limit the number of estimated parameters. Evident transitions in the mechanism are unlikely, as the usual temperature range of intermediate-temperature SOFC is lower than 1118 K.^{94,95} The present study follows the set of limited elementary steps proposed by Zhu et al.⁹⁸



Two situations involving a single RDS are considered, yielding different apparent reaction orders and charge-transfer coefficients

$$j_{tot} = \xi_{TPB_{an}} i_{o_{an}}^{ct} \frac{\left(\frac{x_{H_2}}{\bar{x}_{H_2}}\right)^{1/4} x_{H_2O}^{3/4}}{1 + \left(\frac{x_{H_2}}{\bar{x}_{H_2}}\right)^{1/2}} \left[\exp\left(\frac{3}{2} \frac{F}{RT_s} \eta_{an}^{ct}\right) - \exp\left(-\frac{1}{2} \frac{F}{RT_s} \eta_{an}^{ct}\right) \right] \text{ at } \Gamma_4 \quad [24]$$

$$j_{tot} = \xi_{TPB_{an}} i_{o_{an}}^{ct} \frac{\left(\frac{x_{H_2}}{\bar{x}_{H_2}}\right)^{1/4} x_{H_2O}^{1/4}}{1 + \left(\frac{x_{H_2}}{\bar{x}_{H_2}}\right)^{1/2}} \left[\exp\left(\frac{1}{2} \frac{F}{RT_s} \eta_{an}^{ct}\right) - \exp\left(-\frac{3}{2} \frac{F}{RT_s} \eta_{an}^{ct}\right) \right] \text{ at } \Gamma_4 \quad [25]$$

$$\tilde{x}_{H_2} = \tilde{x}_{o_{an}} \exp\left[-\frac{\tilde{E}_{o_{an}}}{R} \left(\frac{1}{T_s}\right)\right] \quad [26]$$

$\tilde{x}_{H_2} = (a_{(Ni)}^{x_{H_2}})/a_{H_2}^{(Ni)}$ represents the equilibrium of reaction 19 (HO1). Eq. 24 (HO3) and Eq. 25 (HO2) is obtained in case reaction 21 or reaction 20 is rate-limiting, respectively. The derivation of the former is presented by Zhu et al.⁹⁸ That of the latter proceeds similarly.

Modelling of diffusion and chemical processes on the anode side.— The dusty-gas model¹⁰⁰ is solved in one-dimension through the anode support, along with the equation of continuity. It provides the distribution of species molar fraction x_i , molar flux N_i , pressure p_{an} and chemical reaction rates \mathfrak{R}_i . The water-gas-shift reaction is assumed at equilibrium until the interface Γ_4 , between the anode and the electrolyte, whereas steam-methane reforming is computed according to the kinetic approach of Achenbach.⁴⁵ The system of equations to solve is

$$-\frac{\partial}{\partial z}x_i - \frac{x_i}{p_{an}}\frac{\partial}{\partial z}p_{an} - x_i\frac{B_{oan}}{\mu_{gan}D_{iM}^e}\frac{\partial}{\partial z}p_{an} = \sum_{j=1, j \neq i}^n \frac{x_j N_j - x_i N_i}{c_{tan} D_{ij}^e} + \frac{N_i}{c_{tan} D_{iM}^e} \text{ in } \mathcal{R}_3 \quad [27]$$

$$\frac{\partial}{\partial z}p_{an} = \frac{\sum_{j=1}^n N_j}{\frac{1}{RT} + \frac{B_{oan}}{\mu_{gan}} \sum_{i=1}^n \frac{x_i}{D_{iM}^e}} \text{ in } \mathcal{R}_3 \quad [28]$$

$$\frac{\partial}{\partial z}N_i = \mathfrak{R}_i \text{ in } \mathcal{R}_3 \quad [29]$$

$$\text{at } \Gamma_3 : \begin{cases} N_{H_2} = -N_{H_2O} = \frac{j_{tot}}{2F} \\ N_i = 0, i = N_2, CH_4, CO, CO_2 \end{cases} \quad [30]$$

$$\text{at } \Gamma_3 : \begin{cases} x_{ian} = x_i \\ p_{an} = p^{atm} \end{cases} \quad [31]$$

Boundary conditions Eq. 30 assume that the electrochemical processes are restricted to the anode/electrolyte interface. A quick estimate of dimensionless numbers (see e.g. Ref. 44) under typical conditions during stack operation and the different electrode thicknesses (cathode: 60 μm , anode: 540 μm) support the validity of this simplification. The ratios between (i) the ohmic resistivity and the resistivity due to electrochemical reaction and (ii) the resistivity due to electrochemical reaction and mass transfer (Thiele modulus) are around 6 and 1, respectively, for the typical conditions during stack operation. Analysis in Part II with an anode composite electrode model further demonstrates that this simplification captures the alteration of the TPB by nickel particle coarsening; the degradation of the ionic conductivity of the 8YSZ phase in the anode does not dominate. In the Stefan-Maxwell approach for multi-component diffusion both effective Knudsen D_{iM}^e and binary pairs diffusion coefficients D_{ij}^e do not depend on the gas composition¹⁰⁰

$$D_{iM}^e = \frac{n_{an} d_p}{\tau_{an}^2} \sqrt{\frac{8RT_s}{\pi M_i}} \quad [32]$$

$$D_{ij}^e = \frac{n_{an}}{\tau_{an}^2} 1.43 \cdot 10^{-7} T_s^{1.75} \left(\frac{2}{1/M_i + 1/M_j} \right)^{-1} (v_{d_i}^{1/3} + v_{d_j}^{1/3})^{-2} \quad [33]$$

The catalytic activity of the SOFC Ni-YSZ anode for methane steam-reforming is the subject of extensive research. The proposed models range from detailed elementary heterogenous chemical kinetics^{52,101} to simpler empirical relations. The kinetic approaches proposed by Achenbach and Riensche⁴⁵ or Leinfelder¹⁰² are believed to provide a sufficient level of detail in the conditions considered here, even though the temperature range of intermediate-temperature SOFC, i.e. 973–1073 K, is not included in the domain of validity of both relations (see Table I). The relations for the reaction rate \mathfrak{R}_{SMR} can be expressed in a generic form

$$\mathfrak{R}_{SMR} = \frac{k_{oan}^{SMR}}{h_{an}} x_{CH_4}^{r_{an1}^{SMR}} x_{H_2O}^{r_{an2}^{SMR}} \exp \left[-\frac{E_{oan}^{SMR}}{R} \left(\frac{1}{T_s} - \frac{1}{T_{ref}} \right) \right] \text{ in } \mathcal{R}_3 \quad [34]$$

Both expressions^{45,102} do not account for any equilibrium and have been determined as averaged surface reaction rates.

The equilibrium of the water-gas shift reaction is not strictly enforced but approximated by using the following reaction rate

$$\mathfrak{R}_{ws} = k_{oan}^{ws} x_{CO} \left[1 - \frac{(x_{CO_2} x_{H_2}) / (x_{CO} x_{H_2O})}{K_{ws}^{eq}} \right] \text{ in } \mathcal{R}_3 \quad [35]$$

where k_{oan}^{ws} is an arbitrarily high constant.

Cathode.—LSCF and composite LSM-YSZ are the two most common cathode materials used in SOFC stacks. The processes involved in the ORR and degradation, as well as their distributions in these materials differ, which must be correctly implemented in an electrochemical model for degradation simulations at the SRU scale.

In mixed-ionic and electronic conductors (MIEC) with significant ionic conductivity, such as LSCF, the different elementary steps can be spread to a significant distance from the electrode/electrolyte interface, resulting in an overall increase of the effective zone.^{34,103} The incorporation of oxygen ions in the ion-conducting electrode proceeds through surface reaction. The intrinsic properties of MIEC materials place much more importance on determining the ratio between bulk and surface pathways, compared with the Ni-YSZ case. Experiments performed on thick films^{104,105} demonstrated the ionic predominance of the bulk pathway for materials with high ionic conductivity, and the small resistance to charge-transfer across samaria-doped ceria/LSC interfaces.¹⁰⁵ Therefore, the ORR in technological MIEC cathodes might not be necessarily limited by electrochemical kinetics, rather than by chemical elementary steps.

The ORR in LSM is not completely understood, despite extensive research.¹⁰³ The use of composite LSM-YSZ widens the electrochemically active zone. The ionic conductivity of LSM in SOFC conditions is limited, but may exhibit different regimes depending on the overpotential.¹⁰⁶ Tracer experiments on a LSM grid deposited on a YSZ substrate¹⁰⁷ have demonstrated the presence and likely interplay of the bulk and surface pathways. Van Heuveln et al.¹⁰⁸ have investigated the ability of different elementary reaction schemes to reproduce their experimental data on porous LSM electrodes and have proposed that the diffusion of adsorbed O^- species along the LSM surface and charge-transfer co-limit the ORR. Another suggested RDS is oxygen dissociation and adsorption, e.g. Ref. 109. EIS measurements can exhibit up to five possible contributions.¹¹⁰ The dominance and appearance of these contributions in EIS depend among others on manufacturing, test history and measurement conditions. The two high frequency arcs are related to transport and transfer of oxygen intermediates or oxide ions across the LSM-YSZ interface and through the YSZ backbone. The usually dominant and permanent arc located at intermediate frequencies is assumed to reflect separately or combined dissociative adsorption, transfer of species to the TPB and surface diffusion. Two low frequency arcs related to gas diffusion in the stagnant gas layer above the electrode and possibly to impurity segregates at the TPB might appear. Reported apparent reaction orders on oxygen are in the range of 0–1, and activation energies are in the range of 100–200 kJ mol^{-1} for candidate RDS (145–183 kJ mol^{-1} for the usually dominant arc at intermediate frequencies). An activation

Table I. Domain of validity for the parameters proposed by Achenbach and Riensche (Ref. 45) and Leinfelder et al. (Ref. 102).

Parameter	Achenbach et al. (Ref. 45)	Leinfelder et al. (Ref. 102)
T (K)	1073–1273	884–973
SCR (–)	3–8	2
p (Pa)	1.1×10^5 – 2.8×10^5	1.1×10^5
h_{an} (μm)	1400	25
n (–)	0.4	0.3

phenomenon is usually observed during the initial polarisation in performance testing of short stacks. Suggested causes are, among others, the dissolution of undesirable phases from impurities or manufacturing processes,¹¹⁰ or very localised changes in composition and morphology of the TPB.¹¹¹ This behaviour formally poses the question of a reference state for degradation simulations at the SRU scale.

Modelling studies on the underlying mechanisms of the ORR are available in the literature, and can be selected and adapted for SRU models. Adler et al.³⁴ have developed a continuum, one-dimensional model of MIEC electrodes, which focuses on the bulk path. This approach is supported by the large amount of data on bulk diffusion D_v , surface kinetics K_{chem} and deviation from stoichiometry.^{112–119} As pointed out by Adler et al.,¹²⁰ most of this data holds only close to equilibrium, and extrapolation to a large deviation is questionable. Their model enables an estimate of the utilisation length in the electrode, and displays agreement with measurements on good ionic conductors, such as LSC and LSCF.³⁴ The model however fails to represent the behaviour of LSM electrodes. The main reason is the aforementioned possibility of different pathways, which has been investigated by Svensson et al.³⁵ and later by Coffey et al.³⁸ Similar to the case of the anode, these models require a large amount of reliable data, which is their major drawback.³⁸ Another limitation of one-dimensional continuum models arises once the extension of the active zone in the MIEC is similar to the particle size. The utilisation length and current distribution at the MIEC/electrolyte interface depends on the ratio K_{chem}/D_v ,³⁷ and hence they influence current constriction problems.

To our knowledge, MIEC models^{34,35,38} have not yet been adapted and used for simulation at the SRU scale, despite the extensive use of LSCF in intermediate-temperature SOFC. This approach is used in the present study to verify its ability to reproduce experimental data from segmented-cell tests and support the subsequent implementation of degradation phenomena. In the case of LSM-YSZ cathode, the composite electrode model is meant to improve the performance of the electrode.^{9,39,44,121} It provides the local overpotential, gas composition and effect of TPB and ionic conductivity of the YSZ network that are needed to implement degradation processes such as chromium contamination and zirconate formation. The composite electrode model can retrieve information from specific studies on the ORR to implement degradation in the view of altered elementary steps, even though the current understanding of degradation and amount of data for calibration may not yet support such an approach. This emphasises the need for efficient calibration procedures to capture at least the correct dependences and enable a reliable prediction of the local performance and temperature distribution in the SRU.

Cathode composite electrode model.— The composite electrode model of LSM-YSZ cathode assumes that the ORR is restricted to the TPB, while electrons and ions are transported separately in the electronic and ionic phases. The charge balance is solved along with mass transport to provide the distribution potential ($V_{ion,cath}$, $V_{el,cath}$), current density ($j_{ion,cath}$, $j_{el,cath}$) in the ionic and electronic phases as well as oxygen molar fraction x_{O_2} . The charge balance is described by the following system of equations

$$\frac{\partial}{\partial z} V_{ion,cath} = -\rho_{ion,cath}^e j_{ion,cath} \quad \text{in } \mathcal{R}_5 \quad [36]$$

$$\frac{\partial}{\partial z} V_{el,cath} = -\rho_{el,cath}^e j_{el,cath} \quad \text{in } \mathcal{R}_5 \quad [37]$$

$$\eta_{cath} = (V_{ion,cath}^{eq} - V_{el,cath}^{eq}) - (V_{ion,cath} - V_{el,cath}) \quad \text{in } \mathcal{R}_5 \quad [38]$$

$$\frac{\partial^2}{\partial z^2} \eta_{cath} = A_{TPB,cath} (\rho_{el,cath}^e + \rho_{ion,cath}^e) i_{cath} \quad \text{in } \mathcal{R}_5 \quad [39]$$

$$\text{at } \Gamma_5 : \begin{cases} j_{ion,cath} = j_{tot} \\ j_{el,cath} = 0 \end{cases} \quad [40]$$

$$\text{at } \Gamma_6 : \begin{cases} j_{ion,cath} = 0 \\ j_{el,cath} = j_{tot} \end{cases} \quad [41]$$

A percolation theory is used to estimate the TPBL and effective conductivities (see Part II for description⁷⁰).

Eqs. 42–43 are solved for the mass transport, and coupled to the charge-transfer problem by the faradaic transfer current i_{cath}

$$\frac{p_{cath}}{RT_s} \frac{\partial^2 x_{O_2}}{\partial z^2} = \frac{1}{4FD_{O_2}^e} A_{TPB,cath} i_{cath} \quad \text{in } \mathcal{R}_5 \quad [42]$$

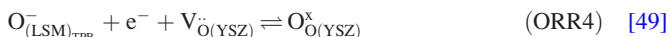
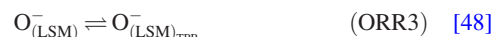
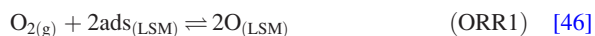
$$\text{at } \Gamma_5 : D_{O_2}^e \frac{\partial x_{O_2}}{\partial z} = 0 \quad [43]$$

$$\text{at } \Gamma_6 : x_{i,cath} = x_i \quad [44]$$

The classical Bosanquet relation is used for the calculation of the effective diffusion coefficient. The calculation of both Knudsen $D_{O_2}^e$ and binary $D_{O_2-N_2}^e$ diffusion coefficients proceed in a similar manner as for the anode

$$\frac{1}{D_{O_2}^e} = \frac{1}{D_{O_2M}^e} + \frac{1}{D_{O_2-N_2}^e} \quad [45]$$

The sequence of elementary processes of van Heuveln et al.^{9,108} for high temperature considers charge-transfer on adsorbed oxygen (ORR2) as RDS



The surface diffusion step (ORR3) possibly co-limiting the ORR at low overpotential is not considered. The derivation of the apparent reaction order and charge-transfer coefficient presented by van Heuveln et al.¹⁰⁸ assumes a low coverage of adsorbed or intermediate oxygen species, which might hold at high temperature and low oxygen partial pressure, but less at low temperature.^{98,122} Hence, a modification is required for intermediate-temperature SOFC. The derivation of the expression for the faradaic transfer current i_{cath} yields

$$i_{cath} = i_{o,cath}^{ct} \frac{\left(\frac{x_{O_2}}{\tilde{x}_{O_2}}\right)^{3/8}}{1 + \left(\frac{x_{O_2}}{\tilde{x}_{O_2}}\right)^{1/2}} \left[\exp\left(-\frac{1F\eta_{cath}}{2RT_s}\right) - \exp\left(\frac{3F\eta_{cath}}{2RT_s}\right) \right] \quad [50]$$

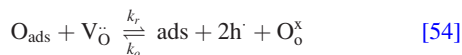
$$i_{o,cath}^{ct} = T_s k_{o,cath} \exp\left[-\frac{E_{a,cath}}{R} \left(\frac{1}{T_s} - \frac{1}{T_{ref}}\right)\right] \quad [51]$$

$\tilde{x}_{O_2} = a_{O_{(LSM)}}^2 / (x_{O_2} a_{(LSM)}^2)$ arises from the equilibrium of Eq. 46 (ORR1) and can be conveniently expressed as

$$\tilde{x}_{O_2} = \tilde{x}_{o,cath} \exp\left[-\frac{\tilde{E}_{a,cath}}{R} \left(\frac{1}{T_s}\right)\right] \quad [52]$$

Cathode MIEC model.— The approach is based on that proposed by Adler et al.³⁴ and Svensson et al.^{35,71} One single path is considered, i.e. the surface adsorption of oxygen at the pore walls of the MIEC, followed by vacancy diffusion through the bulk, and finally direct exchange of vacancies with the electrolyte





The derivation of the model under the assumptions of the present study is recalled here, to highlight the adaptations and nature of required data for the simulation at the SRU scale. The equations for the transport of vacancies c_v in the bulk of the MIEC are derived by considering the MIEC as a moderately-dilute solution,¹²³ containing ion vacancies, electrons and holes. The electrochemical potential μ_e^* is used as the driving force for the bulk diffusion of vacancies. The vacancy flux is

$$N_v = -\frac{D_v c_v}{RT} \frac{\partial \mu_v^*}{\partial z} \quad [56]$$

where μ_v^* , the local electrochemical potential, depends on both the local electrical state and the local composition. The electrochemical potential of the electrons can be arbitrarily used to define a quasi-electrostatic potential Φ

$$\mu_e^* = RT \ln c_e + z_e F \Phi \quad [57]$$

The expression of the gradient of the electrochemical potential of the vacancies can be rewritten as in Ref. 123, assuming the electron-hole pair reaction is at equilibrium³⁴

$$\frac{\partial \mu_v^*}{\partial z} = \frac{\partial}{\partial z} \left(\mu_v^* - \frac{z_v}{z_e} \mu_e^* \right) + \frac{z_v}{z_e} \frac{\partial \mu_e^*}{\partial z} \quad [58]$$

which after inserting Eq. 57 becomes

$$\frac{\partial \mu_v^*}{\partial z} = \frac{\partial}{\partial z} \left[RT \left(\ln c_v - \frac{z_v}{z_e} \ln c_e \right) \right] + \frac{\partial}{\partial z} \left[RT \left(\ln f_v - \frac{z_v}{z_e} \ln f_e \right) \right] + \frac{z_v}{z_e} \frac{\partial \mu_e^*}{\partial z} \quad [59]$$

hence the expression for the vacancy flux N_v

$$N_v = -D_v c_v \frac{\partial}{\partial z} \ln c_v + D_v c_v \frac{z_v}{z_e} \frac{\partial}{\partial z} \ln c_e - D_v c_v \frac{\partial}{\partial z} \left(\ln f_v - \frac{z_v}{z_e} \ln f_e \right) - \frac{z_v}{z_e} \frac{\partial \mu_e^*}{\partial z} \frac{D_v c_v}{RT} \quad [60]$$

$$N_v = -D_v c_v \frac{\partial}{\partial z} \ln c_v \left[1 - \frac{\partial \ln c_e^{\frac{z_v}{z_e}}}{\partial \ln c_v} + \frac{\partial \ln f_{v,e}}{\partial \ln c_v} \right] - \frac{z_v}{z_e} \frac{\partial \mu_e^*}{\partial z} \frac{D_v c_v}{RT} \quad [61]$$

$$N_v = -\mathcal{A} D_v \frac{\partial c_v}{\partial z} - \frac{z_v}{z_e} \frac{D_v c_v}{RT} \frac{\partial \mu_e^*}{\partial z} \quad [62]$$

where \mathcal{A} is defined as:

$$\mathcal{A} = 1 - \frac{\partial \ln c_e^{\frac{z_v}{z_e}}}{\partial \ln c_v} + \frac{\partial \ln f_{v,e}}{\partial \ln c_v} \quad [63]$$

The factor \mathcal{A} is a measurable thermodynamic quantity. Indeed, from the definitions

$$\mu_v^* = \mu_{v,e}^* + RT \ln(f_{v,e} c_v c_e^2) - 2\mu_e^* \quad [64]$$

and

$$\mu_{\text{O}_2}^{\text{chem}} = \mu_{\text{O}_2}^{\text{chem}_o} + RT \ln(p_{\text{O}_2}) \quad [65]$$

and the following relation holds (at the pore wall, at equilibrium, $\frac{1}{4} \mu_{\text{O}_2}^{\text{chem}} = \mu_h^* - \frac{1}{2} \mu_v^*$):

$$\mathcal{A} = \frac{\partial \mu_v^*}{\partial \ln c_v} = -\frac{1}{2} \frac{\partial \ln x_{\text{O}_2}}{\partial \ln c_v} \quad [66]$$

The problem due to the assumptions on the different elementary steps for the oxygen adsorption at the pore wall is overcome by using an apparent exchange coefficient, experimentally determined, close to equilibrium, for common LSCF. The simplified exchange reaction at the MIEC/gas interface is considered as an average volumetric reaction rate $\mathfrak{R}_{\text{MIEC}}$ due to the 1D description

$$\mathfrak{R}_{\text{MIEC}} = \frac{K_{\text{chem}} c_v}{\mathcal{A}} \left(\mathcal{A} \frac{c_v - c_v^{\text{eq}}}{c_v} + \frac{1}{2} \frac{x_i - x_i^{\text{eq}}}{x_i} \right) \quad [67]$$

Simple empirical relations proposed by Yang et al.¹²⁴ are used to estimate the dependence of the exchange coefficient K_{chem} on temperature and oxygen partial pressure in the gas found in literature.¹¹²⁻¹¹⁹ The same applies to the concentration of vacancies at equilibrium in the perovskite c_v^{eq} and the diffusion coefficient D_{chem} (see Table II for values)

$$D_{\text{chem}} = \mathcal{A} D_v = D_o, \exp\left(-\frac{E_{a_e}}{RT}\right) \quad [68]$$

$$K_{\text{chem}} = C_{K_1} \exp\left(-\frac{E_{a_K}}{RT}\right) x_{\text{O}_2}^{C_{K_2} + C_{K_3} T} \quad [69]$$

$$c_v^{\text{eq}} = \frac{\delta}{V_m} = 3C_{\delta_1} \exp\left(-\frac{E_{a_\delta}}{RT}\right) x_{\text{O}_2}^{C_{\delta_2} + C_{\delta_3} T} \quad [70]$$

Insertion of Eqs. 62 and 67 in the vacancy conservation equation, $-\partial N_v / \partial z - A_{\text{MIEC}} \mathfrak{R}_{\text{MIEC}} = 0$, yields the one-dimensional steady-state conservation equation

$$\frac{1 - n_{\text{cath}}}{\tau_{\text{cath}}} \left(\mathcal{A} D_v \frac{\partial^2 c_v}{\partial z^2} + D_i \frac{\partial c_v}{\partial z} \frac{\partial \mathcal{A}}{\partial z} + \frac{z_v}{z_e} \frac{D_v c_v}{RT} \frac{\partial^2 \mu_e^*}{\partial z^2} + \frac{z_v}{z_e} \frac{D_v}{RT} \frac{\partial c_v}{\partial z} \frac{\partial \mu_e^*}{\partial z} \right) - A_{\text{MIEC}} \mathfrak{R}_{\text{MIEC}} = 0 \quad [71]$$

For modelling at the SRU scale, assuming high electronic conductivity of the MIEC, i.e. $\nabla \mu_e^* = 0$ is an acceptable simplification, and $\nabla \mathcal{A} = 0$ is reasonable in the considered range of oxygen partial pressure for the typical MIEC materials used in SOFC, Eq. 71 simplifies to

$$\frac{1 - n_{\text{cath}}}{\tau_{\text{cath}}} \left(\mathcal{A} D_v \frac{\partial^2 c_v}{\partial z^2} \right) - A_{\text{MIEC}} \mathfrak{R}_{\text{MIEC}} = 0 \quad \text{in } \mathcal{R}_s \quad [72]$$

Simplified boundary conditions are

$$j_{\text{tot}} = -2F \frac{1 - n_{\text{cath}}}{\tau_{\text{cath}}} D_{\text{chem}} \frac{\partial c_v}{\partial z} \quad \text{at } \Gamma_5 \quad [73]$$

$$0 = \frac{1 - n_{\text{cath}}}{\tau_{\text{cath}}} D_{\text{chem}} \frac{\partial c_v}{\partial z} \quad \text{at } \Gamma_6 \quad [74]$$

The diffusion problem described previously (Eqs. 42 and 43) still holds, except that $A_{\text{TPB,cath}} i_{\text{cath}}$ has to be replaced by $A_{\text{MIEC}} \mathfrak{R}_{\text{MIEC}}$.

The exchange of vacancies between the MIEC and the electrolyte Eq. 55 formally involves a charge-transfer, but this term is likely not dominant for an LSCF/GDC interface¹⁰³ and therefore neglected in the present study. In the case treated here, i.e direct exchange of vacancies at the interface, the electrode overpotential η_{cath} is related to vacancy concentration by³⁵

$$\eta_{\text{cath}} = -\frac{RT_s}{2F} \ln \frac{c_v|_{\text{MIEC-elect}}}{c_v^{\text{eq}}} \quad [75]$$

Parameter estimation.—gPROMS (Ref. 66) has parameter estimation and design of experiment capabilities. The estimation of

Table II. Values of the fixed parameters and allowable range of the fitted parameters.

Conductivities							
	8YSZ	20GDC	LSM	Ni	MIC, air	MIC, fuel	
$k_{O_{ion}}$	7.92e8 (Ref. 9)	7.04e4 T_s (Ref. 130)	—	—	—	—	
$E_{a_{ion}}$ (kJ mol ⁻¹)	110.0 (Ref. 9)	21.9 (Ref. 130)	—	—	—	—	
$k_{e_{el}}$	50.0 ^a	—	10700 T_s (Ref. 131)	60000 (Ref. 132)	45.8 (Ref. 70)	120.5 (Ref. 70)	
$E_{a_{el}}$ (kJ mol ⁻¹)	—	—	12.9 (Ref. 130)	—	33.3 (Ref. 70)	45.3 (Ref. 70)	
Electrochemical processes							
	k_o^{ct} (A cm ⁻²)	E_a^{ct} (kJ mol ⁻¹)	\tilde{x}_o	\tilde{E}_a (kJ mol ⁻¹)	r_{an1}^{ct}	r_{an2}^{ct}	r_{cath}^{ct}
Anode (HO2)	0.05–100 ^b	60–190 ^b	2.136 (Ref. 52)	96 (Ref. 52)	1/4 ^c	1/4 ^c	—
Anode (HO3)	0.05–100 ^b	60–190 ^b	2.136 (Ref. 52)	96 (Ref. 52)	1/4 ^c	3/4 ^c	—
Anode (EMP)	0.05–100 ^b	60–190 ^b	2.136 (Ref. 52)	96 (Ref. 52)	0–0.5 ^b	0–1.0 ^b	—
Cathode	0.001–20 ^b	80–290 ^b	3.33e9 (Ref. 125)	186 (Ref. 125)	—	—	3/8 ^c
Cathode	0.001–20 ^b	80–290 ^b	4.9e8 (Ref. 122)	200 (Ref. 122)	—	—	3/8 ^c
Chemical reactions in porous media							
	τ^2	n	d_p	k_{SMR}^{SMR}/h_{an}	E_{SMR}^{SMR} (kJ mol ⁻¹)	r_{an1}^{SMR}	r_{an2}^{SMR}
Anode	6–14 ^b	0.31 ^d	6.98e-7 ^d	0.053 (Ref. 45)	82 (Ref. 45)	1	0
Anode	6–14 ^b	0.31 ^d	6.98e-7 ^d	32.255 (Ref. 102)	205 (Ref. 102)	1	1
Cathode	3 ^e	0.42 (Ref. 15)	4.4e-7 (Ref. 15)	—	—	—	—
Electrode morphology							
	ϕ_{el}	ϕ_{ion}	$d_{g_{el}}$	$d_{g_{ion}}$	τ_s	l_g^h	d_g^h
Anode	0.4 (Ref. 127)	0.6 (Ref. 127)	1.25e-6 (Ref. 127)	1.15e-6 (Ref. 127)	—	9e-7	1e-7
Cathode	0.49	0.51	4.5e-7 (Ref. 15)	3.5e-7 (Ref. 15)	3 ^f	9e-7	1e-7
MIEC surface properties							
	A_{MIEC} (cm ⁻¹)	C_{K_1}	C_{K_2}	C_{K_3}	E_{a_k} (kJ mol ⁻¹)		
LSCF	20000 (Ref. 34)	1.805 (Ref. 117)	2.0611 (Ref. 117)	–0.00142 (Ref. 117)	98.3 (Ref. 117)		
MIEC bulk properties							
	V_m	C_{δ_1}	C_{δ_2}	C_{δ_3}	$E_{a_{\delta}}$ (kJ mol ⁻¹)	D_{o_e}	E_{a_e} (kJ mol ⁻¹)
LSCF	34.09	39.30 (Ref. 116)	–0.772 (Ref. 116)	5.04e-4 (Ref. 116)	77.1 (Ref. 116)	0.0497 (Ref. 117) 0.0050–0.1 ^b	159.6 (Ref. 117)
Geometry							
	$Elect$	cl	$Cath$	an	GDL_{an}	GDL_{cath}	MIC
H (DLR)	7e-6	7e-6	60e-6	540e-6	0.95e-3	0.95e-3	6e-3 ^g
H (EPFL)	7e-6	7e-6	60e-6	540e-6	1.00e-3	2.00e-3	2e-3

^aASR value, (Ω cm²).

^bFitting parameter, range in parameter estimations.

^cFrom model assumption.

^dMercury porosity measurement performed at DLR.

^eAveraged value, no strong influence in the conditions of the calibration.

^fValue merged with D_{o_e} during the parameter estimations.

^gHeight of segment.

^hFor current constriction calculation, contact geometry with electrolyte estimated from [Ref. 18].

the parameters θ_i is achieved in the form of an optimisation problem, where the objective function Ψ is based on the normal probability distribution (its natural logarithm) and accounts for the experimental data (\mathcal{N}_{exp} and \mathcal{N}_{resp} , including repetitions \mathcal{N}_{rep}).

$$\Psi = \frac{\mathcal{N}}{2} \ln(2\pi) + \frac{1}{2} \min_0 \sum_k \left\{ \sum_i \sum_j \left[\ln(s_{ij}^2) + \frac{(\hat{y}_{ij} - y_{ij})^2}{s_{ij}^2} \right] \right\}_k \quad [76]$$

where y and \hat{y} are respectively the simulated and measured system responses. This objective function takes into account the variance in the measurements s_{ij} . Indeed, the residuals are weighted by their variance, and therefore, favored for their increased reliability. A constant variance model is used.

gPROMS (Ref. 66) provides three main indicators that should be used together to evaluate the adequacy of the model: (i) lack-of-fit test, (ii) F-test and (iii) statistical significance of the estimated parameters. The computation of joint confidence regions to assess the

reliability of parameter estimates is based on a linear approximation of the parameter variance-covariance matrix.

Experimental

The calibration of the models is performed on current-voltage (IV) characteristics measured by means of two different segmented-cell test rigs, the detailed description of which is provided elsewhere.^{67,68} Only the key features of the experiments are discussed here.

The two setups are designed for different purposes. The first one, developed at the German Aerospace Center (DLR) aims at studying the variation of SOFC characteristics over a generic geometry,⁶⁷ while the second, developed at LENI-EPFL, aims at identifying and mitigating issues related to a specific SRU design.⁶⁸ This implies different arrangements of the segments (see in Figs. 1a and 1b). The present study takes advantage of the capability of segmented tests to gather simultaneously a large amount of data for different currents, potentials, temperatures and gas compositions. The ease of data

processing and suitability for parameter estimation slightly differ in favour of the DLR setup, owing to the continuous arrangement of the segments, better uniformity of the fuel flow and increased gas-tightness of the cathode compartment.

In the present case of an anode-supported cell, only the cathode is segmented. An anode-supported cell (ASC2) (InDec, Netherlands) has been tested in the DLR setup. It consisted of a 540 μm thick anode and a 7 μm YDC compatibility layer on top of the 7 μm 8YSZ electrolyte. The thickness of the LSCF cathode along with its current collection layer was 60 μm . An anode compensating layer was added to reduce the curvature of the cell. A similar anode support has been tested in the LENI-EPFL setup, but with a LSM-YSZ composite cathode (HTceramix, Switzerland), screen-printed on the 8YSZ electrolyte.

The DLR setup can accommodate cells of 100 cm^2 . The active area for measurements is 73.8 cm^2 , divided into 16 electrically-isolated segments of 4.6 cm^2 , equally distributed over the active area of the SRU (see Fig. 1b). Gases are supplied in either co- or counter-flow configuration. Mixtures of H_2 , H_2O , CO , CO_2 , CH_4 and N_2 can be fed into the anode compartment, within the safe ranges to prevent carbon deposition, limited by the maximum achievable amount of steam of 3%. The molar fraction of O_2 in the cathode gas can be varied as well.

The LENI-EPFL setup is based on the SRU design developed within the FlameSOFC project.^{7,8,68,72} The shape of the SRU with an active area of 200 cm^2 is depicted in Fig. 1a, along with the arrangement of 18 segments of 1.7 cm^2 . Local measurements are not performed on the remaining active area, reduced to 133 cm^2 , due to the implementation of the segmentation. Experiments are carried out with air, while nitrogen-diluted or not, wet or dry hydrogen is fed on the fuel side.

The typical operating conditions applied during both tests and used for model calibration here are listed in Table III.

Investigated Cases

The following model variations are tested against the experimental data:

- Three different approaches for the description of the electrochemical processes on the anode side, one empirical (referred to as EMP, Eq. 17) and two based on different RDS (Eq. 24, HO3 and Eq. 25, HO2).
- Two different sets of parameters for the calculation of \tilde{x}_{O_2} (Eq. 52) (Refs. 122 and 125).

Table III. Range of operating conditions included in the parameter estimations.

	DLR setup	LENI-EPFL setup
Operating time (h)	75–400	15–23
Furnace temperature (K)	973–1073	1057–1062
Air inlet temperature (K)	973–1073 ^a	1043
E (V)	0.575–1.07	0.7–1.05
j_{Umax} (A cm^{-2})	1.2	0.7
Air flow (nmllpm cm^{-2})	20–80	9.62 ^b
Fuel flow (nmllpm cm^{-2})	6.25–25	7.3–11.0
Anode inlet molar fractions	—	—
H_2	0.1–0.97	0.5–0.97
H_2O	0–0.03	0.03
N_2	0–0.9	0–0.5
CH_4	0.02–0.1 ^c	0
Cathode inlet molar fraction	—	—
O_2	0.05–0.5	0.21

^a Assumed identical to the furnace temperature.

^b Air ratio.

^c Not included in parameter estimation.

- Two empirical relations (Eq. 34 and Table I) for internal steam-methane reforming in SOFC anodes, from Achenbach and Rienesche⁴⁵ and Leinfelder et al.¹⁰²

The particularities of the two setups imply distinct processing strategies. The data gathered by the DLR setup is more extensive in terms of measurement points and conditions. Four units of the one-dimensional model with the electrochemical model for a MIEC cathode material are assembled in y-direction to model one single row of segments (see Fig. 1b). The setting of the inlet gas flow rate assumes a uniform distribution. To partially overcome this simplification, the calculation of the variance includes the responses recorded on the two central rows. The available specific variations of temperature, gas flow rates, and anode and cathode gas compositions are spread over a time period of 325 h. Degradation phenomena therefore affect the accuracy of the calibration. The approach pursued here is not meant to clarify the reasons for the degradation, but seeks to avoid the overestimation of parameters affected by operating conditions varied at the end of the measurement campaign.

Two degradation phenomena among those considered in Part II (Ref. 70) are applied to correct the data for the observed overall degradation. The decrease of ionic conduction of the electrolyte and of electronic conduction of the uncoated MIC due to corrosion are the less sensitive to test history, which enable to avoid the computational burden that would result from the simulation of the complete experiment for all parameter estimation runs, i.e. IV characterisation and aging. Results with and without application of the correction for degradation are compared.

The data from LENI-EPFL is smaller in amount and affected by experimental contingencies, such as a marked local degradation at the inlet of the SRU due to contamination of the cathode from volatile species transported by the air, and small deficiencies in the anode flow field.^{68,72} As a result, only data from segment 2, 3 and 4 are suitable for the present study. The discontinuous experimental discretisation of the central line (segments 1–6) prevents the straightforward use of the one-dimensional modular model for the in-plane direction, as the local current density is not resolved in the main area. Therefore, averaged conditions over the segments are computed by a 2D model⁷ and applied as local conditions on the electrochemical model alone. An ohmic resistance is added in the inlet area delimited by segment 1 to coarsely model the large initial degradation in this one and to prevent an underestimation of the hydrogen molar fraction on the downstream segments.

The choice of the fitting parameters, as listed in Table II, is dictated by considerations on the possible dedicated experiments, which could improve the calibration procedure. The following parameters are fixed according to data from literature, despite the scatter in the reported values:

- The electronic and ionic conductivities of all materials ($k_{\text{Oion}}, E_{\text{aion}}, k_{\text{Oel}}, E_{\text{ael}}$).
- The morphological parameters of the electrode, only those of the cathode being all explicitly required in the present study, to compute the effective conductivities and TPBL ($r_{\text{el}}, r_{\text{ion}}, \varphi_{\text{el}}, \varphi_{\text{ion}}, l_{\text{g}}, d_{\text{g}}, n, d_n$).
- The tortuosity of the porous and solid network in the cathode (τ_{cath}).
- One set of parameters for the calculation of \tilde{x}_{H_2} (Eq. 26), two sets for \tilde{x}_{O_2} (Eq. 52).
- Two different sets of parameters for the steam-methane reforming reaction ($k_{\text{Oan}}^{\text{SMR}}, E_{\text{aan}}^{\text{SMR}}, r_{\text{an1}}^{\text{SMR}}, r_{\text{an2}}^{\text{SMR}}$) (Eq. 34 and Table I).
- The dependence on temperature and oxygen partial pressure of the surface (Eq. 69) and bulk (Eq. 68) properties of the LSCF cathode material ($E_{\text{av}}, E_{\text{aK}}, C_{\text{K}_2}, C_{\text{K}_3}$) (Fig. 4).
- The parameters for the calculation of the deviation from stoichiometry in the LSCF cathode ($C_{\delta_1}, C_{\delta_2}, C_{\delta_3}, E_{\delta_6}$) (Eq. 70 and Fig. 4).
- The internal surface area of the LSCF cathode (A_{MIEC}).

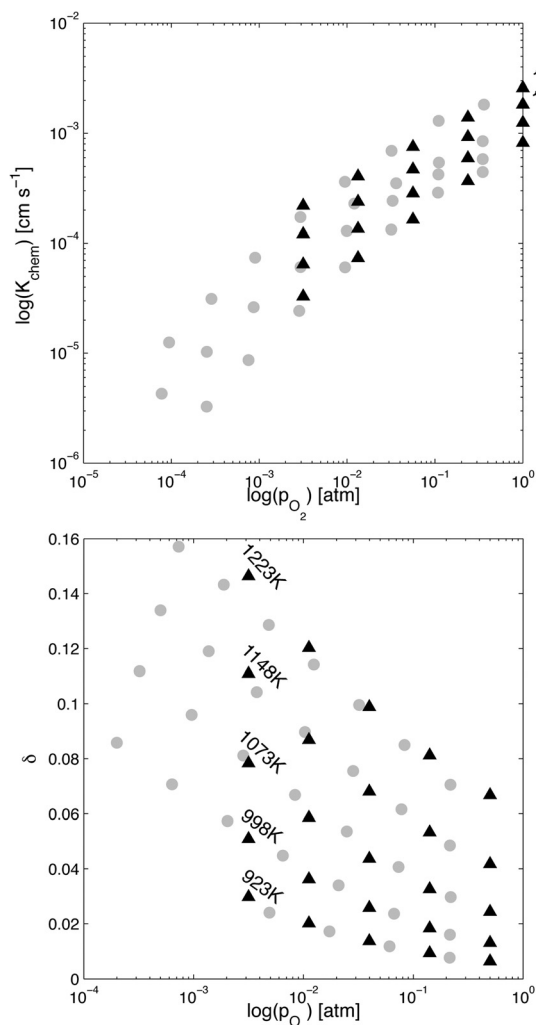


Figure 4. Comparison between experimental (gray dots) (Refs. 116 and 117) and implemented (black triangles) properties of LSCF, as computed by Eq. 69 (top) and Eq. 70 (bottom).

The fitting parameters are therefore:

- The parameters for the description of the electrochemical processes in the anode: k_{an}^{ct} and E_{an}^{ct} for HO3 and HO2, r_{an1}^{ct} , r_{an2}^{ct} are added for the empirical relation EMP (Eq. 17).
- The parameters for the description of the electrochemical processes in the cathode (Eq. 50), k_{cath}^{ct} and E_{cath}^{ct} .
- The pre-exponential factor for the diffusion of vacancies (D_{ov}) (Eq. 68).

The ratio of the surface to bulk properties is a key value which controls the extension of the active zone in an electrode made of a MIEC material.^{34,37} Therefore, while D_{ov} is fitted, C_{K1} is accordingly varied, constrained by the ratio K_{chem}/D_{chem} . Figure 4 depicts the surface properties and deviation from stoichiometry implemented in the model.

The calibration sequence starts with the data gathered by the DLR setup. Parameter estimation runs are first performed on measurements with hydrogen as fuel, with the three anode models (EMP, HO2, HO3).

They do not include all experiments. Those left are used to verify afterwards the reliability of the calibrated model. Measurements with internal steam-methane reforming are sparse and the variations limited by the maximum amount of steam of 3%. Therefore, the parameters of the empirical relation Eq. 34 are not estimated. The data is used to discriminate between the parameters provided by Achen-

bach and Riensche⁴⁵ or Leinfelder et al.¹⁰² Owing to the similar anode support used in all experiments, the data from LENI-EPFL are used to estimate only the parameters of the cathode composite model. The calibration is performed separately with the three previously calibrated anode models (EMP, HO2 and HO3).

The differences in behaviour between the three anode models and two cathode materials are assessed at the SRU level on a one-dimensional description of the non-segmented version of the SRU depicted in Fig. 1a. Adiabatic boundary conditions are set, inducing temperature differences exceeding 100 K, typical of a SRU embedded in a stack.

Results and Discussion

Parameter estimation, case of LSCF cathode.—The variance in the measurements affects the information conveyed by the experiments. Its assessment is required to evaluate the adequacy of a model and whether the quality of the data is sufficient to discriminate between different models. Imprecision in the data from DLR used for parameter estimation originates both from limitations of the experimental setup and the degradation, because of the choice of the measurement sequence.

Figure 5 depicts the IV curves measured on the two central rows of the DLR setup, for different gas flows and hydrogen inlet molar fractions, from 2 to 50%, at 1073 K. The onset of limitation shifts towards lower current densities, along the flow path, due to the depletion of hydrogen. The conditions yielding the highest current densities in Fig. 5 are referred to as the nominal operating point: the furnace temperature is 1073 K, and air (80 nmlpm cm^{-2}) and 50% diluted wet hydrogen (25 nmlpm cm^{-2}) are fed in the cathode and anode compartments, respectively. Measurements in these conditions are available at four different operating times. The degradation causes a maximum decrease of the cell voltage of approximately 55 mV during the time period from 136 to 377 h depicted in Fig. 5. The corresponding value of the variance is used for the parameter estimation, whether correction for the degradation is applied or not on the data. A comparison in Fig. 5 of the response of segments located at identical positions along the flow path shows that the measurement error can be potentially much smaller. An analysis of the error induced by the sensors and control could be sufficient in the case of

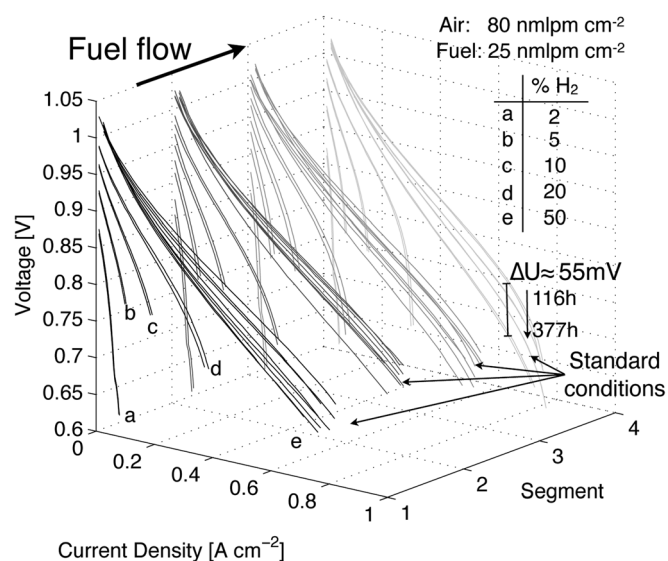


Figure 5. IV characteristics measured with the DLR setup (LSCF cathode), for different gas flows and inlet molar fractions of hydrogen, from 2 to 50%, at 1073 K (see Table III). The indications refer to the inlet conditions in the SRU. Standard conditions: air 80 nmlpm cm^{-2} , fuel 3% humidified H_2 : N_2 50:50. The curves appear in pairs, corresponding to the 2 central segment rows.

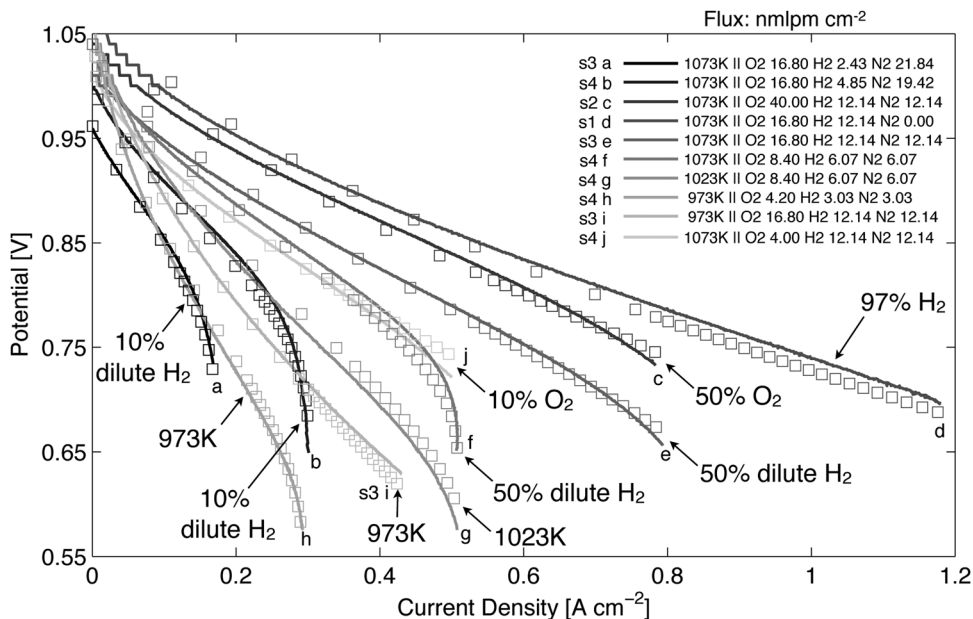


Figure 6. Comparison between experimental (lines) and simulated (squares) IV characteristics for various conditions. DLR data. HO2 anode model, calibrated on data corrected for the degradation. Gas flow is nlpm cm^{-2} , s = segment number (Fig. 1b).

an experimental sequence optimised for model calibration, which would vary the parameter of interest within short time periods. In the present case, the degradation affects the measurements and the dataset does not allow to characterise its effect for all conditions. Because the present understanding of degradation is incomplete and the dataset does not allow to characterise its effect over the whole range of investigated parameters, the constant variance model is used, even though the response at the nominal conditions depicted in Fig. 5 suggests an heteroscedastic variance model might be required. The degradation does not drastically affect the pattern of the measured IV characteristics over the considered time period. This allows to correct the data for model calibration purpose only by implementing degradation phenomena inducing an increase of the ohmic losses, as discussed in the section on Investigated cases, even though other processes may be involved.

Figure 6 provides a comparison between the experimental data from various segments and the predictions provided by the HO2 model, calibrated with a correction for the degradation (see also

Fig. 7). The agreement is acceptable over a wide range of local conditions which are representative of those in a SOFC stack. The emphasis in the parameter estimation runs is placed on the effect of the temperature and anode gas composition on the cell response, as in most cases a high air ratio is required for the thermal management of a functional stack. Experiments with the lowest inlet oxygen molar fraction of 0.02 are not fitted satisfactorily (not depicted), despite the validity of Eqs. 68–70 in this range (see Fig. 4). Difficulties concern mainly the detection of the onset of limitation. An unlikely high tortuosity of the gas phase in the cathode is required to reproduce the data. One reason is the one-dimensional discretisation of the cathode, which cannot capture local oxygen depletion caused by the geometry of the GDL system, when coupled to a thin electrode. The range over which the calibration is acceptable remains however wide enough to ensure a reliable prediction of the behaviour of a functional SRU, to show the relevance of a MIEC model at the SRU scale and to confirm the dependences included in Eqs. 68–70 (see later).^{116,117}

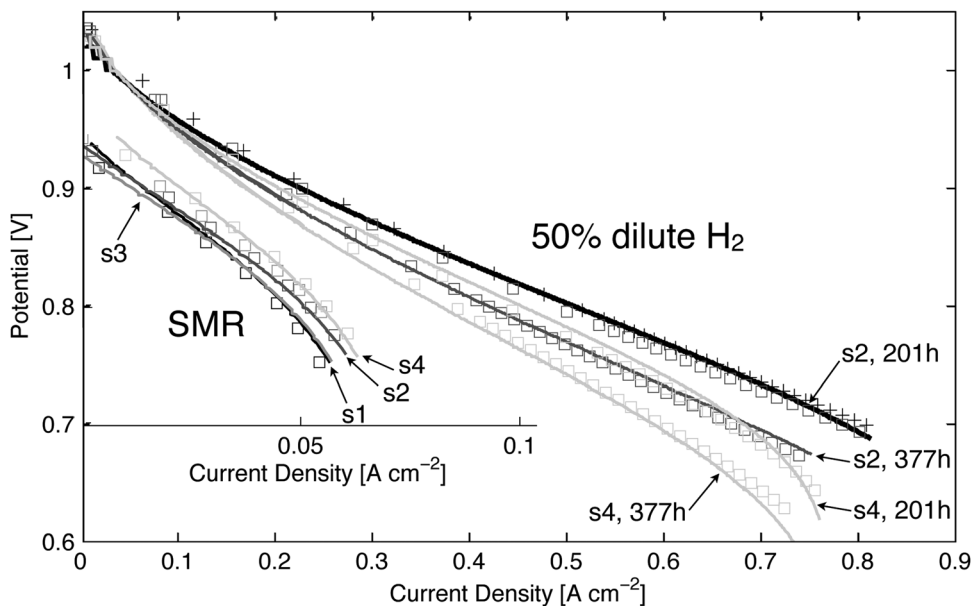


Figure 7. Effect of the correction for the degradation and internal steam-methane reforming. HO2 anode model. Case of LSCF cathode (DLR data). The effect of correction for the degradation is shown for the standard conditions (boxes, compare $t = 201$ h and $t = 377$ h). The simulation from calibration without correction is depicted for $t = 201$ h (crosses). The experiments including internal steam-methane reforming (SMR insert) are simulated with the HO2 model and the kinetic relation from Achenbach et al.⁴⁵

Table IV. Results of the parameter estimations with the DLR data. LSCF cathode. Inside parentheses are the 90% confidence interval and standard deviation.

Anode model	EMP	
	W/o correction	Correction
Ψ	-4930.5	-4990.7
$E_{a_{an}}^{ct}$ (kJ mol ⁻¹)	113.3 (8.4, 5.1)	109.5 (10.4, 6.4)
$k_{a_{an}}^{ct}$ (A cm ⁻²)	13.26 (3.12, 1.90)	21.69 (6.02, 3.66)
r_{an1}^{ct}	0.46 (0.06, 0.04)	0.29 (0.07, 0.05)
r_{an2}^{ct}	0.52 (0.04, 0.02)	0.62 (0.06, 0.04)
τ_{an}^2	8.13 (1.46, 0.89)	12.86 (0.78, 0.48)
D_{O_2} (cm ² s ⁻¹)	186.3 (54.0, 32.8)	206.2 (54.8, 33.3)
Anode model	HO2	
	W/o correction	Correction
Ψ	-4851.6	-4943.5
$E_{a_{an}}^{ct}$ (kJ mol ⁻¹)	153.1 (7.1, 4.3)	131.1 (9.3, 5.6)
$k_{a_{an}}^{ct}$ (A cm ⁻²)	5.95 (0.54, 0.33)	13.46 (1.68, 1.02)
τ_{an}^2	12.99 (0.34, 0.20)	13.35 (0.32, 0.20)
D_{O_2} (cm ² s ⁻¹)	141.4 (17.7, 10.8)	137.6 (16.5, 10.0)
Anode model	HO3	
		Correction
Ψ		-4935.1
$E_{a_{an}}^{ct}$ (kJ mol ⁻¹)		133.0 (11.6, 7.1)
$k_{a_{an}}^{ct}$ (A cm ⁻²)		12.60 (3.45, 2.10)
τ_{an}^2		13.66 (0.33, 0.20)
D_{O_2} (cm ² s ⁻¹)		163.2 (48.8, 29.6)

Table IV lists the results of the parameter estimations, for the three anode models and correction or not for the degradation. The values of the objective function ψ are directly comparable, as the same dataset is used for all calibrations. The lowest objective function, i.e. the best fit, is obtained with the EMP model, with a correction of the data for the degradation. The two other models based on physical assumptions on the anode RDS (HO2 and HO3) yield comparable results in terms of overall quality. All runs listed in Table IV successfully pass the statistical model adequacy tests. The choice of the fitting parameters, such as constraining the temperature dependence of the ratio K_{chem}/D_{chem} and the use of a reference temperature (Eqs. 18, 34, and 51) prevent high correlations between the parameters. The optimal values, along with their confidence intervals, fall within the ranges reported in the literature: 70–170 kJ mol⁻¹ for the activation energy on the anode side $E_{a_{an}}^{ct}$, -0.5 to 1.0 for the apparent reaction orders on hydrogen r_{an1}^{ct} and 0.3–1.0 for the apparent reaction orders on steam r_{an2}^{ct} . The estimated tortuosity around 3.6 is slightly higher than expected.¹²⁶ Possible reasons are the one-dimensional discretisation that does not account for the geometry of the GDL system and the presence of the contacting and compensating layers. The fitted value lumps the mass transfer resistance of all functional layers and that of the GDL. The EMP model yields slightly lower values of the tortuosity, since r_{an1}^{ct} and r_{an2}^{ct} modify the apparent onset of diffusion limitation. The optimal values of 0.29 and 0.62 for r_{an} are close to those set in the HO3 model (0.25 and 0.75).

The computed 90% confidence intervals are between 2 and 25% of the estimated value. These do however not contain the optimal value of all other parameter estimation runs. The tightest intervals, between 2 and 12%, are obtained with the HO2 model, with correction of the data, partly due to the reduced number of estimated parameters. The different models predict comparable contributions of the cathode, expressed by D_{O_2} in Table IV, and consequently of the anode.

The implementation of a correction for the degradation reduces the objective function. The data gathered at the beginning of the test, around 100–200 h, have been preferentially selected for the parameter estimation runs, since it corresponds to the time at which

the effect of anode and cathode gas composition have been tested. Variation of the furnace temperature has been performed only after 400 h of operation on a degraded cell (see Fig. 5). Figure 7 shows the effect of the correction for the degradation on IV characteristics for the standard operating conditions, recorded at 201 and 377 h. Simulation with (squares) and without (crosses) correction for the degradation show acceptable agreement with the IV characteristic at 201 h, which is included in the data for parameter estimation. That recorded at 377 h is used here to verify the validity of the correction for the degradation. The overall trend is well reproduced, but the subtle changes in the onset of diffusion limitation are not modelled. If the data is not corrected, the additional degradation ensuing operation induces a higher estimated activation energy for the hydrogen oxidation (113–153 kJ mol⁻¹ instead of 110–133 kJ mol⁻¹), since the temperature dependence of all contributions, except that of the anode, are fixed.

Operation with methane achieves higher efficiency than with hydrogen. While internal steam-methane reforming can be beneficial for the thermal management of the stack, structural issues can arise from its endothermic nature. A calibration under these conditions of higher technological relevance is essential to ensure the reliability of a SRU model. The DLR setup does not comprise an evaporator, which limits the achievable testing conditions with methane. The data is too sparse in amount to estimate reliably the parameters of Eq. 34. Instead, the parameters listed in Table I are discretely tested. The data is characterised by low current densities due to the steam molar fraction limited to 3%. The IV characteristics simulated with the relation from Achenbach and Riensche⁴⁵ provided better agreement with measurements than the relation from Leinfelder et al.¹⁰² The choice of an anode electrochemical model does not drastically alter the simulated responses, despite the differences in the apparent reaction orders on hydrogen and steam. The EMP model achieves a slightly better agreement. Figure 7 includes the comparison between measurements and simulations with the relation from Achenbach and Riensche,⁴⁵ without any specific adjustment of the parameters. Unlike experiments carried out with hydrogen as fuel, the current density increases along the flow path, as methane is progressively reformed. The model correctly captures this trend. Figure 8 shows the simulated distribution of methane and hydrogen in the anode, along a row of segments, for the operating points characterised by the highest current density in Fig. 7. The molar fraction of

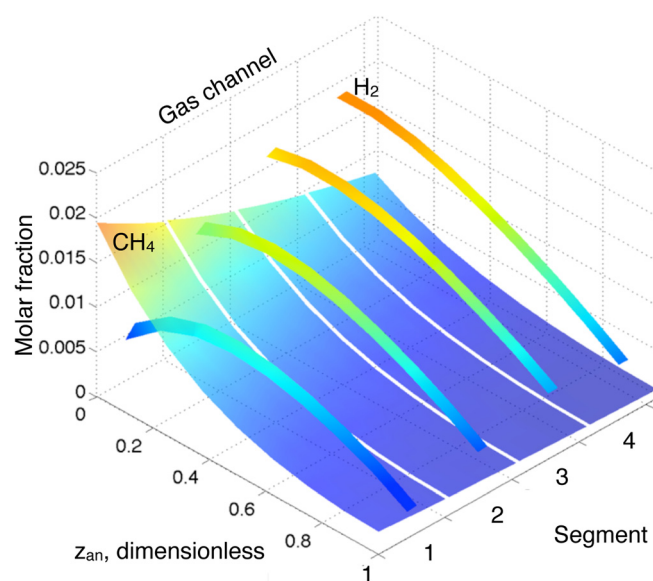


Figure 8. (Color online) Distribution of the hydrogen (ribbons) and methane molar fractions in the anode, along the flow path, as predicted with the HO2 model, coupled to the relation for steam-methane reforming from Achenbach et al.⁴⁵ The operating point is that of highest current density in Figure 7.

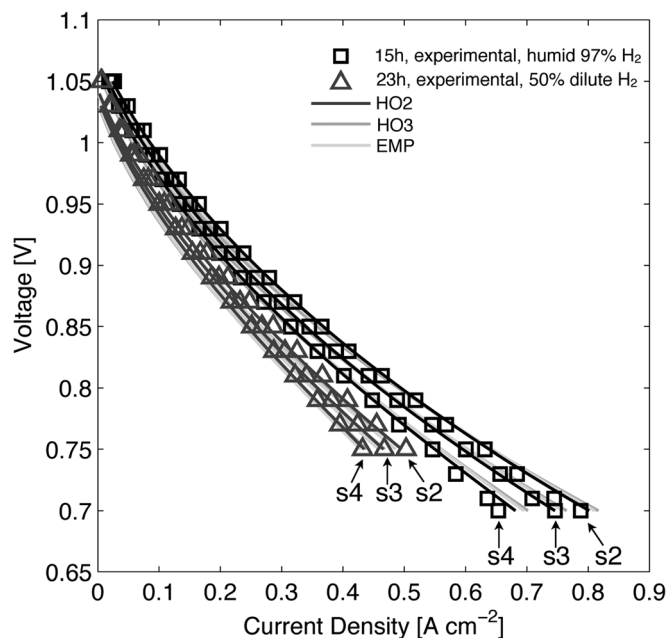


Figure 9. Comparison between experimental (squares, triangles) and simulated (lines) IV characteristics used for the calibration of the LSM-YSZ model, EPFL-LENI setup, segments s2,s3,s4 (Fig. 1a).

methane decreases along the flow path in the gas channel and towards the interface. That of hydrogen, depicted by the ribbons, exhibits a maximum in the anode in the upstream segment and overall increases along the flow path, which accounts for the higher potential at the outlet. The results confirm that acceptable predictions of the behaviour under internal steam reforming can be achieved with a simplified modelling approach, based on the electrochemical conversion of hydrogen, coupled to an empirical kinetic relation for the steam-methane reforming. A better calibration of the models requires an additional measurement campaign, on a setup equipped with an evaporator. The level of accuracy is believed sufficient for degradation simulation, since the effect of anode gas composition on nickel particle coarsening is not yet completely understood and precisely characterised over the whole range found in SOFC stack.^{12,127}

The quality of a fit cannot completely assess the validity of a model. Previous calibrations with simpler models, the terms of which lack a strict physical meaning, such as Wilcke formulation for diffusion losses on the anode side, or Butler-Volmer equation to describe the electrochemical processes in the LSCF cathode, produced satisfactory agreement with part of the dataset shown in Fig. 6, except for significant discrepancies that occurred for the highest hydrogen dilutions. However, they are of limited interest for the mitigation of degradation in SOFC stacks under practical operating conditions, since they could not reproduce the cell response under internal steam-reforming conditions and their nature does not enable the implementation of degradation phenomena.

Parameter estimation, case of LSM-YSZ cathode.—The LENI-EPFL experiment is design-oriented. The gas manifold is identical to that of a functional stack. Issues related to the anode flow affected the measurements and have been subsequently addressed.⁶⁸ The present study overcomes this limitation by using the values of the anode parameters estimated with the DLR data, because the anode support is the same in both experiments. Another drawback of the LENI-EPFL experiment for the present study is the difficulty to vary the oxygen molar fraction on the cathode side precisely and over a wide range. This is inherent to the setup, which has an air manifold dimensioned for a stack and consequently increased relative gas leaks in SRU testing configuration.

Figure 9 shows the results of the parameter estimation. The agreement between experimental data and simulation is acceptable. All curves exhibit the same pattern, as only the measurements on the central segments, 2–4 (see Fig. 1a), are usable. The differences between the two experiments carried out after 15 and 23 h of operation are the dilution and flux of the anode gas. Despite the fixed furnace and gas inlet temperature, the temperature range in the data is of approximately 20 K, owing to the polarisation and locations of the segments.

Table V lists the results of the parameter estimations. The limited amount of data induces large confidence intervals and a high correlation between the parameters. The HO2 model, along with the parameters from Matsuzaki et al.¹²⁵ for the calculation of \bar{x}_{O_2} , achieves the lowest objective function Ψ . The optimal values of the cathode activation energy (140–161 kJ mol⁻¹) fall within the range of 100–200 kJ mol⁻¹ reported in the literature.

Simulations of the behaviour of a repeating unit.—The results of the parameter estimations do not allow discriminating between the different models: the objective function is the lowest for the EMP model, and acceptable predictions can still be obtained without a correction of the data for the degradation. Further investigations, with the help of design of experiment theories, are required to determine whether the data gathered by the kind of experiments used in the present study convey enough information for model discrimination. In the present view of lifetime extension and identification of structural failures in SOFC stacks, it is crucial to verify if the choice of a model critically affects the prediction of the field variables driving the degradation phenomena included in Part II,⁷⁰ over the range of local conditions found in a SRU in operation. Acceptable agreement between simulations and experiments and optimal values of some parameters within the range of physical meaning do not guarantee that the effect of the estimated parameters do not compensate each other and result in inconsistent model behaviour. The model behaviour must be checked to avoid incoherent relative contribution to the polarisation losses and unrealistic prediction of the electrode utilisation length.

Figure 10 compares the simulated response of the SRU shown in Fig. 1c, embedded in a stack, with a cell based on a LSM-YSZ or LSCF cathode, operated in co- or counter-flow configuration. The case of partially pre-reformed methane fed in the SRU (see Table VI) is considered, as it tests all the features of the model and induces the largest variety of local conditions. The air ratio is coarsely adjusted to limit the maximum local solid temperature to 1100 K in the SRU for both co- and counter-flow cases, at a fuel utilisation of 0.8–0.85. The behaviour is barely affected by the choice of an anode

Table V. Results of the parameter estimation performed on the experimental data from the LENI-EPFL setup (LSM-YSZ). Inside parentheses are the 90% confidence interval and standard deviation.

Model	EMP	EMP
\bar{x}_{O_2}	Jiang et al. (Ref. 122)	Matsuzaki et al. (Ref. 125)
Ψ	– 522.3	– 531.9
$E_{a, cath}^{ct}$ (kJ mol ⁻¹)	161.4 (69.8, 42.2)	150.5 (70.1, 42.4)
$k_{o, cath}^{ct}$ (A cm ⁻²)	0.0553 (0.100, 0.061)	0.1377 (0.251, 0.152)
Model	HO2	HO2
\bar{x}_{O_2}	Jiang et al. (Ref. 122)	Matsuzaki et al. (Ref. 125)
Ψ	– 546.6	– 552.9
$E_{a, cath}^{ct}$ (kJ mol ⁻¹)	157.0 (65.7, 39.8)	140.2 (66.0, 39.9)
$k_{o, cath}^{ct}$ (A cm ⁻²)	0.1492 (0.255, 0.154)	0.0530 (0.091, 0.055)
Model	HO3	HO3
\bar{x}_{O_2}	Jiang et al. (Ref. 122)	Matsuzaki et al. (Ref. 125)
Ψ	– 512.6	– 524.5
$E_{a, cath}^{ct}$ (kJ mol ⁻¹)	159.0 (66.2, 40.0)	147.9 (66.5, 40.2)
$k_{o, cath}^{ct}$ (A cm ⁻²)	0.0510 (0.086, 0.053)	0.1329 (0.229, 0.139)

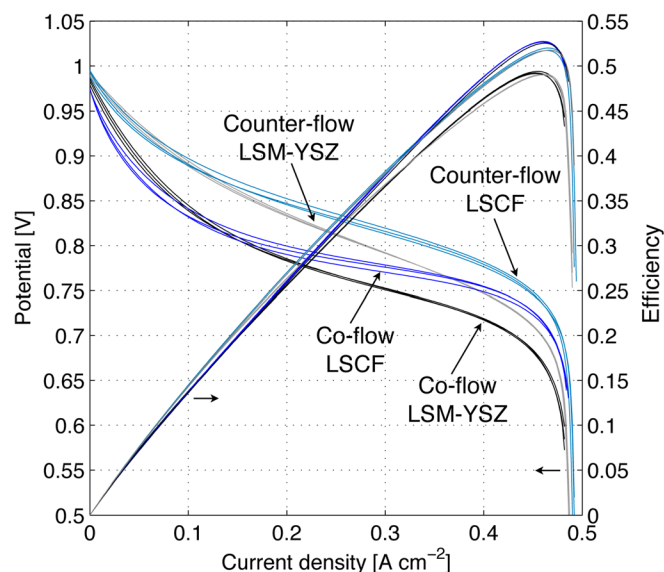


Figure 10. (Color online) IV characteristics of SRUs embedded in a stack, for different flow configurations and cathode materials. Curve series correspond to the three anode models. Stack conditions see Table VI.

model. The LSCF cathode has a better performance than LSM-YSZ, which complies with experimental evidences (e.g. Ref. 30). The same applies to the comparison between counter- and co-flow configuration, at the cost, however, of a higher air ratio for the former (Table VI). The endothermic steam-methane reforming amplifies the gain of the counter- over co-flow, compared with hydrogen as fuel. Indeed, the distribution of the current density follows a trade-off in the co-flow configuration, between highest temperature (low ohmic and electrochemical resistances) and depleted fuel (low local Nernst potential and high anode diffusion losses), both located at the air outlet of the active area. The air inlet side of the active area is lower than the air inlet temperature of 973 K in co-flow (see also Fig. 12). In counter-flow, highest temperature and hydrogen-rich fuel are available at the same location, which coincides with the highest SMR reaction rate. At a fuel utilisation of 0.8, the temperature difference over \mathcal{R}_{area} (see Fig. 1a), for the case of a LSCF cathode, is of 148 K in co-flow, against 115 K in counter-flow. The noticeable decay of the potential at low current density is due to the evolution of the maximum temperature which increases from 950 to 1203 K (co-flow, LSM-YSZ cathode), as the polarisation proceeds. Direct measurement of the cathode gas-phase tortuosity is achievable,¹²⁶ but had to be assigned here, since it was not available here. The cathode gas-phase tortuosity (τ^2) has not been included in the estimated parameters, because of its low anticipated effect. A drastic change from 3 to 5 results in a maximum change in

Table VI. Operating conditions for the SRU simulations.

Air inlet temperature (K)	973
Fuel inlet temperature (K)	973
Fuel flow (nmlpm cm^{-2})	3.6
Air ratio	5–7.5 ^a
Inlet molar fractions	
H ₂	0.263
H ₂ O	0.493
CH ₄	0.171
CO	0.029
CO ₂	0.044

^aValue coarsely adjusted to yield a similar maximum solid temperature of 1100 K at $FU = 0.8$, in co-flow, respectively counter-flow.

predicted potential during IV characterisation in the range of 6 mV and is therefore not depicted. An accurate value of this physical parameter, as well as the choice of a diffusion model for the cathode side are not critical in the present conditions. The estimated value of D_{O_2} includes the effect of porosity and tortuosity on the bulk properties of LSCF cathode.

Figure 11 provides the details of the contribution of the cathode and the Nernst potential, including resistance to mass transfer in the electrode, for the cell with LSCF and LSM-YSZ cathode, respectively. The difference between the anode models is consistent with the optimal values of D_{O_2} listed in Table IV. The cathode performance in the calibrated EMP model is the highest. Figure 12 shows how the zone of highest current density moves towards the fuel inlet at the highest fuel utilisation in co-flow, which induces different trends in the evolution of the ASR of the cathode in co- and counter-flow configurations. In the co-flow case, this shifts results in a monotonic increase of the local temperature all over the active area. In contrast, in the counter-flow case, the local temperature decreases at the end of the IV characterisation, over approximately the first half of the SRU, from the air inlet. This phenomenon in turn amplifies the relative increase of the local current density at the fuel inlet.

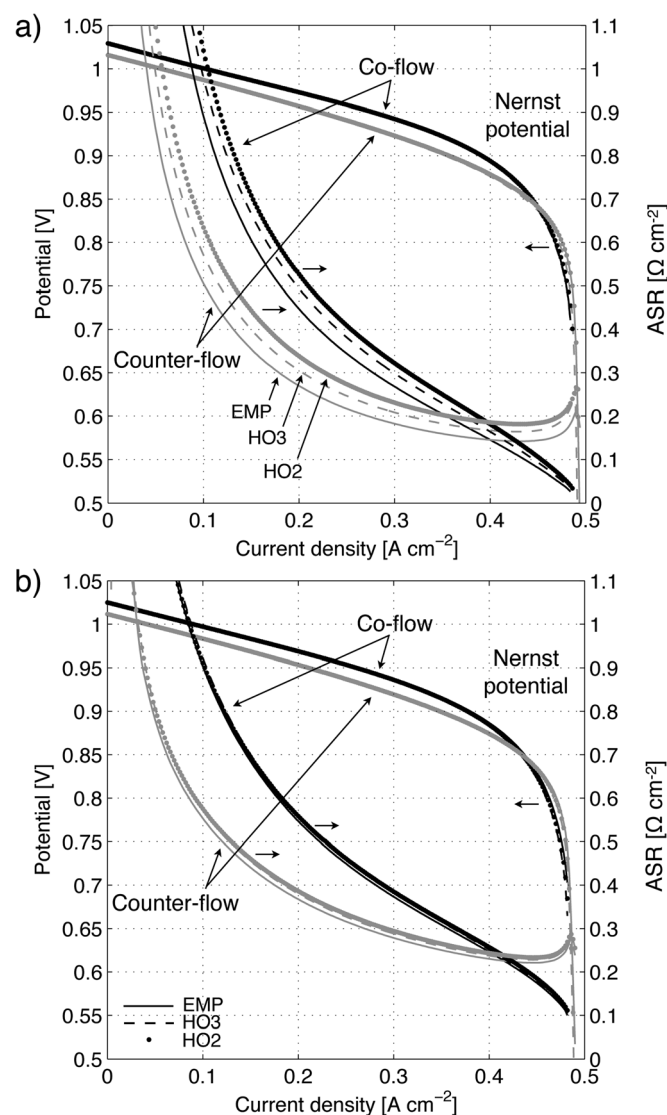


Figure 11. Contributions of the cathode to the ASR and Nernst potential, along with mass transfer resistance, during an IV characterisation of a SRU embedded in a stack. (a) anode-supported cell with LSCF cathode, (b) anode-supported cell with LSM-YSZ cathode.

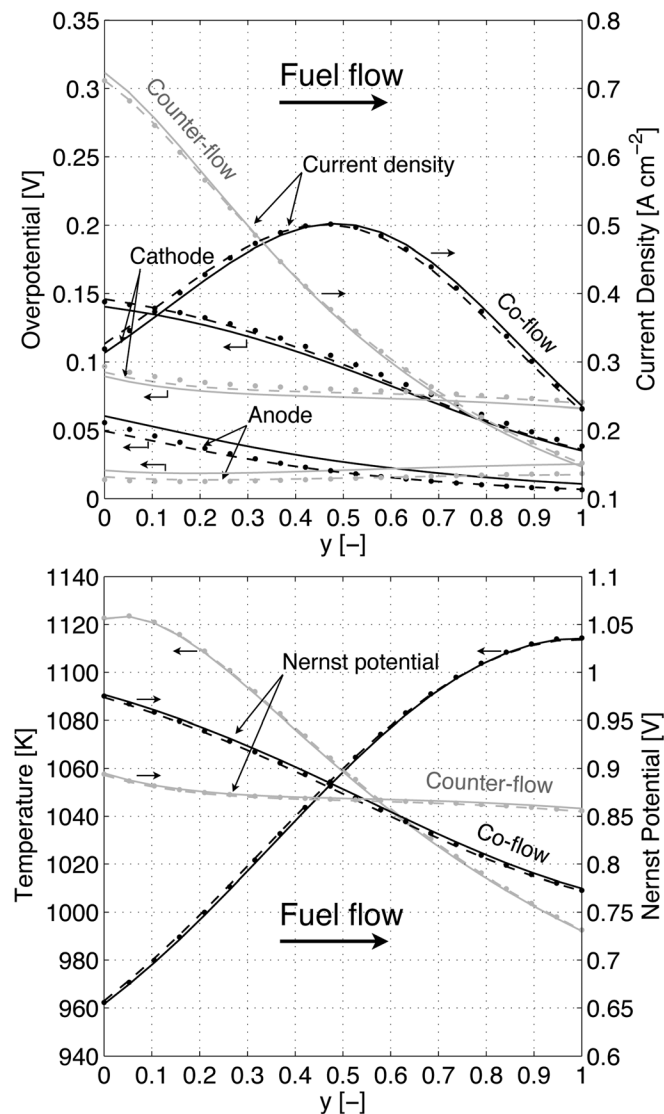


Figure 12. Top: distribution of the overpotential due to electrochemical processes on the cathode and anode side, and current density. Bottom: distribution of the Nernst potential, including diffusion, and temperature over \mathcal{R}_{area} . Case of LSM-YSZ cathode. The fuel utilisation is of 0.8, corresponding to 0.405 A cm^{-2} . The temperature difference is of 152 and 116 K in co- (black) and counter flow (gray), respectively.

The onset of diffusion limitation is higher and shifted towards lower fuel utilisation in co-flow, compared with counter-flow, owing to the distribution of the Nernst potential and lower rate of the steam-methane reforming reaction in the anode in the zone of highest current density.

The design of a SRU in the view of its long-term performance relies on the prediction of the distribution of the field variables driving the degradation. The modelling approach described in Part II (Ref. 70) assumes a predominant effect of the overpotential on the risks of formation of lanthanum (LZO) or strontium zirconates (SZO) and chromium contamination in a LSM-YSZ cathode, as suggested by recent studies.^{18,128} Figure 12 shows the distribution over the active area \mathcal{R}_{area} of the anode and cathode contributions, and Nernst potential, computed at the interfaces between the electrolyte and electrodes, Γ_4 and Γ_5 . The fuel utilisation is 0.8 and the corresponding temperature differences over the active area are 152 and 116 K in co- and counter-flow, respectively. The fuel flow direction is kept constant. Thus, the zone of highest temperature is inverted

between co- and counter flow. The discrepancy between the profiles predicted by the different anode models is small. The contribution of the ORR on the cathode side to the overall losses consistently exceeds that of electrochemical processes on the anode side, over the whole active area, which complies with the typical pattern observed in EIS measurements of anode-supported cells.^{68,128} In contrast to the distribution of the current density, that of the Nernst potential and cathode overpotential is less uniform in the co-flow configuration. The local degradation rate cannot, however, be deduced from the profile of the overpotential, as the degradation phenomena have their own temperature dependence. Nickel particle coarsening, MIC corrosion, release rate of contaminating volatile chromium species from the MIC and thermodynamic risk of formation of LZO/SZO in the LSM-YSZ system are promoted by increasing the temperature [Part II (Ref. 70)]. Even though the respective effects of the current density and overpotential on the degradation are not yet clarified, this observation shows that designing a SRU to

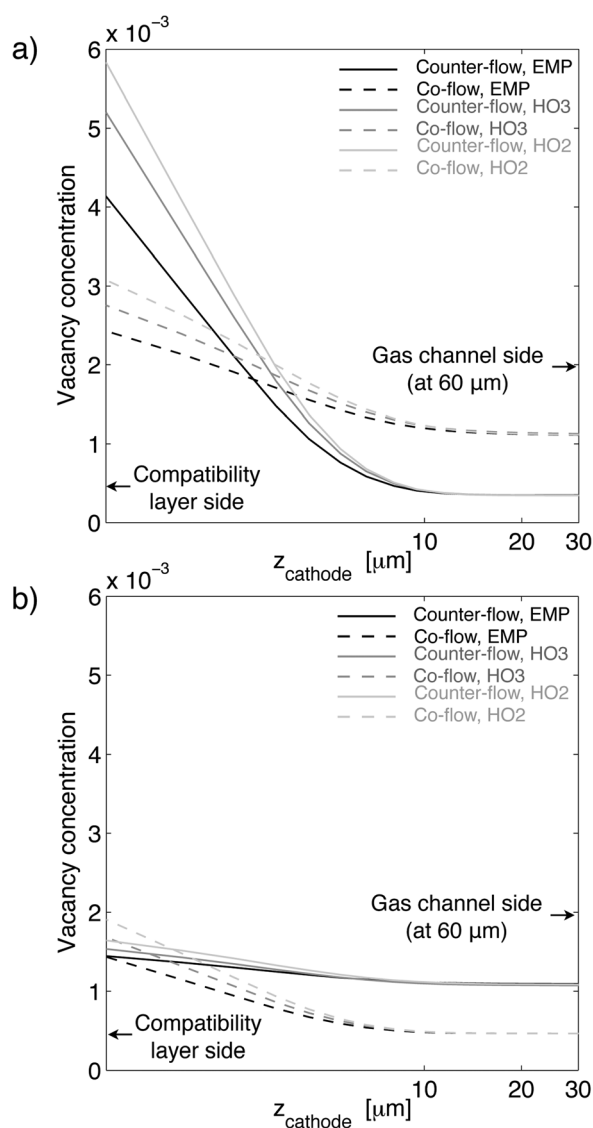


Figure 13. Profile of the vacancy concentration in LSCF cathode, depending on flow configuration, location and anode model. (a) Fuel inlet side of the active area, (b) fuel outlet side of the active area. The first $30 \mu\text{m}$ from the cathode/YDC compatibility layer interface are depicted in logarithmic scale. The cathode/air channel interface is $30 \mu\text{m}$ farther from the indication. The fuel utilisation is 0.8, corresponding to 0.405 A cm^{-2} . The temperature difference is 152 and 116 K in co-flow and counter flow, respectively.

ensure an even current distribution can lead to misleading conclusions, depending on the dominant degradation phenomena.

The extension of the active zone in a cathode made of MIEC material depends on the ratio K_{chem}/D_v .³⁷ Figure 13 shows the extension predicted by the model is in the range of 10 μm , as deduced from the profile of the vacancy concentration c_v within the electrode. This falls within the range of 2–22 μm reported in the literature³⁴, for other materials. The value of K_{chem}/D_v is determined from the data found in the literature (see Table II), due to the choice of the fitting parameters. Therefore, an anode model does not alter the computed extension, but significantly affects the calculated concentration of vacancies at the interface between the cathode and the electrolyte. The MIEC model contains three activation energies for the calculation of the deviation from the stoichiometry, the diffusion of vacancies in the bulk of the cathode and the reaction at the pore wall. The effect of E_{a_δ} is seen in the value of c_v close to the gas channel. The value of the two others, E_{a_K} and E_{a_v} , are comparable, which, together with the high air ratio that limits the oxygen molar fraction gradient over the active area, yields a uniform distribution of the extension of the active zone. The deviation from stoichiometry enables the calculation of local isothermal expansions, which can lead to structural failure, depending on the type of cell and presence or not of localised zones of dramatically low oxygen content, due to a defective sealing concept.¹²⁹

Conclusion

The underlying mechanisms of the electrochemical reactions in SOFCs have not yet been identified unambiguously. Impurities in the raw starting materials could be a reason for the large scatter in the results reported by different groups. This context highlights the need for efficient calibration procedures of SRU and stack models. The approach pursued in this study consists in using two large existing experimental datasets, gathered on two different segmented setups, for the estimation of the parameters of a physical electrochemical model, the refinement of which is sufficient to support the further implementation of degradation phenomena (Part II of this study⁷⁰).

The agreement between model predictions and measurements is satisfactory in both the cases of LSM-YSZ and LSCF cathode, over a wide range of operating conditions. This result shows the relevance of the existing models for electrodes made of a MIEC material available from literature^{34,35} for simulations at the SRU scale. The optimal values of the parameters, along with their confidence interval, lie within the ranges reported in literature. This result, as well as the successful statistical tests, ascertains their physical meaning. The empirical kinetic relation from Achenbach and Rien-sche⁴⁵ achieves reasonable agreement with the experimental data under internal steam-reforming conditions, without specific adjustment of the parameters. Further investigations could not be performed, since the amount of data is insufficient for parameter estimation, because the test setups are not equipped with an evaporator. The applied correction for degradation can quantitatively capture the evolution of the potential. It increases the quality of the fits and relevance and versatility of the proposed tool, since it prevents the undesirable adjustment of some estimated parameters to compensate for degradation.

Fits of acceptable quality are achievable, however, also with models lacking a solid physical ground used elsewhere. The failure of the attempt here to discriminate between physical model assumptions illustrates the limitations of the information conveyed by polarisation curves. A drastic improvement in the calibration procedure could be obtained from a better interrelation between the experiments and modelling. For instance, the effects of degradation could be avoided by selecting another sequence of experiments, while the design of the setup can help to reduce uncertainties caused by the averaging of local conditions. Therefore, additional work involving design of experiment theory will be able to assess the real capabilities of the present approach.

The behaviour of the electrochemical model implemented in a one-dimensional SRU model does not exhibit any significant inconsistencies. The variations in the assumptions of the model do not drastically alter the prediction of the overall performance and local values of the cathode overpotential, which is suspected to govern the degradation of LSM-YSZ cathodes.

Acknowledgments

This work was funded by the Swiss SOFC Consortium, co-financed by the Swiss Federal Office of Energy (SFOE), contract number 152210 and Suisselectric Research. The author would like to thank warmly Nicola Bundschuh for porosimetry measurements on anode supports and Arne Vogel (LBO-EPFL) for his contribution on the parameter estimation Prof. T. Kawada (Tohoku University), Prof. J. Brouwer (UCI), and Shigehisa Kasahara (UNCTAD) for careful reading of the manuscript. gPROMS, a modelling tool from Process System Enterprise (PSE) has been used under academic licensing.

List of Symbol

Latin letters

A	thermodynamic factor
ASR	area specific resistance ($\Omega \text{ m}^2$)
A	area (m^2)
a	surface coverage of adsorption site or adsorbed species
A_{TPB}	specific area at the triple phase boundary ($\text{m}^2 \text{ m}^{-3}$)
A_{MIEC}	internal area of a porous electrode (m^2)
B_o	permeability in porous medium (m^2)
C	constant
c_h	heat capacity (J K^{-1}) kg^{-1}
c_i	molar concentration of species i (mol m^{-3})
c_t	total molar concentration (mol m^{-3})
D	diffusion coefficient in solid medium ($\text{m}^2 \text{ s}^{-1}$)
d_g	particle diameter (m)
d_p	pore diameter (m)
D_{ij}^e	effective bulk diffusivity of binary pair in porous medium ($\text{m}^2 \text{ s}^{-1}$)
D_{iM}^e	effective Knudsen diffusivity of species i in porous medium ($\text{m}^2 \text{ s}^{-1}$)
dH_o	enthalpy of reaction (J mol^{-1})
E	electric potential (V)
E_a	activation energy (J mol^{-1})
F	Faraday's constant 96485 (C mol^{-1})
f	molar activity coefficient
H	enthalpy (J kg^{-1})
h	thickness (m)
h^c	convection heat transfer coefficient ($\text{W m}^{-2} \text{ K}^{-1}$)
i_o	exchange current density (A m^{-2})
i_t	faradaic transfer current density (A m^{-2})
j	current density (A m^{-2})
K^{eq}	equilibrium constant
k_o	kinetic constant
K_{chem}	apparent surface exchange coefficient (m s^{-1})
L	length (m)
l_g	distance between grains (m)
M_i	molecular weight of species i (kg mol^{-1})
\mathcal{N}	number of measurements
n	porosity
N_i	molar flux of species i ($\text{mol m}^{-2} \text{ s}^{-1}$)
p	pressure (Pa)
p^{atm}	atmospheric pressure 101325 (Pa)
p_i	partial pressure (Pa)
\dot{Q}	rate of volumetric thermal energy change (W m^{-3})
\mathcal{R}	computation domain
\mathfrak{R}_i	rate of production of species i ($\text{mol m}^{-3} \text{ s}^{-1}$)
\mathfrak{R}_i^m	rate of production of species i ($\text{kg m}^{-3} \text{ s}^{-1}$)
R	universal gas constant 8.314 ($\text{J mol}^{-1} \text{ K}^{-1}$)
r	apparent reaction order
s	variance
T	temperature (K)
t	time (s)
T_{amb}	ambient temperature, 298 (K)

T_{ref}	reference temperature, 873 (K)	DGM	dusty gas model
u	gas velocity (m s^{-1})	EIS	electrochemical impedance spectroscopy
V	potential in ionic or electronic conducting phases (V)	GCI	galvanostatic current interruption
V_m	molar volume ($\text{m}^3 \text{mol}^{-1}$)	GDC	gadolinia-doped ceria
x_i	mole fraction of species i	GDL	gas diffusion layer
y	system response	HO	hydrogen oxidation
z_i	charge number of species i	IV	current-voltage
Greek letters		LSCF	lanthanum strontium cobaltite ferrite
α	symmetry coefficient	LSM	lanthanum strontium manganite
δ	deviation from stoichiometry	LZO	lanthanum zirconate
η	overpotential (V)	MEA	membrane electrode assembly
ε	emissivity	MIC	metallic interconnect
Γ	domain boundary	MIEC	mixed-ionic-electronic conductor
λ	thermal conductivity ($\text{W m}^{-1} \text{K}^{-1}$)	Ni-YSZ	nickel-YSZ anode in reduced state
μ^*	electrochemical potential (J mol^{-1})	ORR	oxygen reduction reaction
μ^{chem}	chemical potential (J mol^{-1})	RDS	rate-determining step
μ_g	viscosity (Pa s)	SCR	steam-to-carbon ratio
v_d	diffusion volume (m^3)	SMR	steam-methane reforming reaction
ω	mass fraction of species i	SRU	single repeating unit
Φ	potential [V]	SZO	strontium zirconate
ϕ	volume fraction	TPBL	triple phase boundary length
Ψ	objective function	TPB	triple phase boundary
ρ	density (kg m^{-3})	WS	water-gas shift reaction
ρ^e	effective electrical resistivity (Ωm)	YDC	yttria-doped ceria
σ^e	effective electrical conductivity (S m^{-1})	YSZ	yttria-stabilised zirconia
ζ	Stefan-Boltzmann constant $5.670 \cdot 10^{-8}$ ($\text{W m}^{-2} \text{K}^{-4}$)		
τ	tortuosity		
θ	parameter		
ξ	correction factor		
Indices			
a	anodic		
an	anode		
avg	average		
bc	boundary conditions		
c	cathodic		
$cath$	cathode		
cl	compatibility layer		
$cond$	conduction		
$conv$	convection		
$elchem$	electrochemical		
e	electron		
el	electronic		
$elect$	electrolyte		
exp	experiment		
$fnce$	furnace		
g	indice for gases, either air or fuel		
h	hole		
htl	heat losses		
ion	ionic		
isl	insulation		
$leak$	leakage		
o	initial, dense state		
rep	repetition		
$resp$	response		
rx	reaction		
s	index for solid parts, individual components or averaged structure		
tot	total		
u	useful		
v	oxygen vacancy		
Superscripts			
a	anodic		
CT	charge-transfer		
ct	charge transfer		
c	cathodic		
e	effective		
eq	equilibrium		
Acronyms			
ASC	anode-supported cell		
ASR	area specific resistance		

References

- N. Autissier, F. Palazzi, F. Marechal, J. Van herle, and D. Favrat, *J. Fuel Cell Sci. Technol.*, **4**, 123 (2007).
- D. Larrain, J. Van herle, F. Maréchal, and D. Favrat, *J. Power Sources*, **131**, 304 (2004).
- C. Stiller, B. Thorud, O. Bolland, R. Kandepu, and L. Imsland, *J. Power Sources*, **158**, 303 (2006).
- F. Mueller, R. Gaynor, A. E. Auld, J. Brouwer, F. Jabbari, and G. S. Samuelsen, *J. Power Sources*, **176**, 229 (2008).
- M. Fardadi, F. Mueller, and F. Jabbari, *J. Power Sources*, **195**, 4222 (2010).
- C.-K. Lin, T.-T. Chen, Y.-P. Chyou, and L.-K. Chiang, *J. Power Sources*, **164**, 238 (2007).
- A. Nakajo, Z. Willemin, J. Van herle, and D. Favrat, *J. Power Sources*, **193**, 203 (2009).
- A. Nakajo, Z. Willemin, J. Van herle, and D. Favrat, *J. Power Sources*, **193**, 216 (2009).
- B. Kenney and K. Karan, *Solid State Ionics*, **178**, 297 (2007).
- L. C. R. Schneider, C. L. Martin, Y. Bultel, D. Bouvard, and E. Siebert, *Electrochim. Acta*, **52**, 314 (2006).
- A. Hagen, R. Barfod, P. V. Hendriksen, Y. L. Liu, and S. Ramousse, *J. Electrochem. Soc.*, **153**, A1165 (2006).
- L. Holzer, B. Iwanschitz, Th. Hocker, B. Münch, M. Prestat, D. Wiedenmann, U. Vogt, P. Holtappels, J. Sfeir, A. Mai et al., *J. Power Sources*, **196**, 1279 (2011).
- L. Holzer, B. Münch, B. Iwanschitz, M. Cantoni, Th. Hocker, and Th. Graule, *J. Power Sources*, In Press.
- A. Faes, A. Hessler-Wyser, D. Presvytes, C. G. Vayenas, and J. Van herle, *Fuel Cells*, **9**, 841 (2009).
- P. Tanasini, M. Cannarozzo, P. Costamagna, A. Faes, J. Van herle, A. Hessler-Wyser, and C. Comminellis, *Fuel Cells*, **9**, 740 (2009).
- D. Simwonis, F. Tietz, and D. Stöver, *Solid State Ionics*, **132**, 241 (2000).
- A. Mitterdorfer and L. J. Gauckler, *Solid State Ionics*, **111**, 185 (1998).
- Y. L. Liu, A. Hagen, R. Barfod, M. Chen, H. J. Wang, F. W. Poulsen, and P. V. Hendriksen, *Solid State Ionics*, **180**, 1298 (2009).
- M. Chen, Y. L. Liu, A. Hagen, P. V. Hendriksen, and F. W. Poulsen, *Fuel Cells*, **9**, 833 (2009).
- Y. L. Liu and C. Jiao, *Solid State Ionics*, **176**, 435 (2005).
- M. Hattori, Y. Takeda, Y. Sakaki, A. Nakanishi, S. Ohara, K. Mukai, J. H. Lee, and T. Fukui, *J. Power Sources*, **126**, 23 (2004).
- C. C. Appel, N. Bonanos, A. Horsewell, and S. Linderoth, *J. Mater. Sci.*, **36**, 4493 (2001).
- E. Konyshva, J. Mertens, H. Penkalla, L. Singheiser, and K. Hilpert, *J. Electrochem. Soc.*, **154**, B1252 (2007).
- T. Horita, Y. P. Xiong, M. Yoshinaga, H. Kishimoto, K. Yamaji, M. E. Brito, and H. Yokokawa, *Electrochem. Solid-State Lett.*, **12**, B146 (2009).
- S. P. Jiang, J. P. Zhang, L. Apateanu, and K. Foger, *J. Electrochem. Soc.*, **147**, 4013 (2000).
- S. P. Jiang, J. P. Zhang, and K. Foger, *J. Electrochem. Soc.*, **147**, 3195 (2000).
- S. P. Jiang, J. P. Zhang, and K. Foger, *J. Electrochem. Soc.*, **148**, C447 (2001).
- K. Hilpert, D. Das, M. Miller, D. H. Peck, and R. Weiß, *J. Electrochem. Soc.*, **143**, 3642 (1996).
- S. Koch, P. V. Hendriksen, M. Mogensen, Y. L. Liu, N. Dekker, B. Rietveld, B. de Haart, and F. Tietz, *Fuel Cells*, **6**, 130 (2006).
- L. G. J. de Haart, J. Mougín, O. Posdziech, J. Kiviaho, and N. H. Menzler, *Fuel Cells*, **9**, 794 (2009).
- D. Larrain, J. Van herle, and D. Favrat, *J. Power Sources*, **161**, 392 (2006).

32. F. Mueller, F. Jabbari, R. Gaynor, and J. Brouwer, *J. Power Sources*, **172**, 308 (2007).
33. J. Van herle, D. Larrain, N. Autissier, Z. Wuillemin, M. Molinelli, and D. Favrat, *J. Eur. Ceram. Soc.*, **25**, 2627 (2005).
34. S. B. Adler, J. A. Lane, and B. C. H. Steele, *J. Electrochem. Soc.*, **143**, 3554 (1996).
35. A. M. Svensson, S. Sunde, and K. Nisancioğlu, *J. Electrochem. Soc.*, **145**, 1390 (1998).
36. J. Fleig and J. Maier, *J. Eur. Ceram. Soc.*, **24**, 1343 (2004).
37. J. Fleig, *J. Power Sources*, **105**, 228 (2002).
38. G. W. Coffey, L. R. Pederson, and P. C. Rieke, *J. Electrochem. Soc.*, **150**, A1139 (2003).
39. S. H. Chan, X. J. Chen, and K. A. Khor, *J. Electrochem. Soc.*, **151**, A164 (2004).
40. D. Bouvard and F. F. Lange, *Acta Metall. Mater.*, **39**, 3083 (1991).
41. D. Chen, Z. Lin, H. Zhu, and R. J. Kee, *J. Power Sources*, **191**, 240 (2009).
42. J. R. Izzo, A. S. Joshi, K. N. Grew, W. K. S. Chiu, A. Tkachuk, S. H. Wang, and W. Yun, *J. Electrochem. Soc.*, **155**, B504 (2008).
43. A. S. Joshi, K. N. Grew, A. A. Peracchio, and W. K. S. Chiu, *J. Power Sources*, **164**, 631 (2007).
44. P. Costamagna, P. Costa, and V. Antonucci, *Electrochim. Acta*, **43**, 375 (1998).
45. E. Achenbach and E. Riensche, *J. Power Sources*, **52**, 283 (1994).
46. M. A. Khaleel, Z. Lin, P. Singh, W. Surdoval, and D. Collin, *J. Power Sources*, **130**, 136 (2004).
47. P. Aguiar, C. S. Adjiman, and N. P. Brandon, *J. Power Sources*, **138**, 120 (2004).
48. P. Aguiar, C. S. Adjiman, and N. P. Brandon, *J. Power Sources*, **147**, 136 (2005).
49. S. Campanari and P. Iora, *J. Power Sources*, **132**, 113 (2004).
50. F. P. Nagel, T. J. Schildhauer, S. M. A. Biollaz, and S. Stucki, *J. Power Sources*, **184**, 129 (2008).
51. F. P. Nagel, T. J. Schildhauer, S. M. A. Biollaz, and A. Wokaun, *J. Power Sources*, **184**, 143 (2008).
52. R. J. Kee, H. Zhu, and D. G. Goodwin, *Proc. Combust. Inst.*, **30**, 2379 (2005).
53. W. G. Bessler, J. Warnatz, and D. G. Goodwin, *Solid State Ionics*, **177**, 3371 (2007).
54. G. Schiller, W. G. Bessler, K. A. Friedrich, S. Gewies, and C. Willich, *ECS Trans.*, **17**(1), 79 (2009).
55. P. Metzger, Friedrich K. A., G. Schiller, and C. Willich, *J. Fuel Cell Sci. Technol.*, **6**, 021304 (2009).
56. W. G. Bessler, S. Gewies, C. Willich, G. Schiller, and K. A. Friedrich, *Fuel Cells*, **10**, 411 (2010).
57. H. Zhu and R. J. Kee, *J. Power Sources*, **117**, 61 (2003).
58. R. Suwanwarangkul, E. Croiset, M. W. Fowler, P. L. Douglas, E. Entchev, and M. A. Douglas, *J. Power Sources*, **122**, 9 (2003).
59. F. N. Cayan, S. R. Pakalapati, F. Elizalde-Blancas, and I. Celik, *J. Power Sources*, **192**, 467 (2009).
60. V. M. Janardhanan, V. Heuveline, and O. Deutschmann, *J. Power Sources*, **172**, 296 (2007).
61. T. X. Ho, P. Kosinski, A. C. Hoffmann, and A. Vik, *Int. J. Hydrogen Energy*, **34**, 3488 (2009).
62. A. Chaisantikulwat, C. Diaz-Goano, and E. S. Meadows, *Comput. Chem. Eng.*, **32**, 2365 (2008).
63. G. M. Goldin, H. Zhu, R. J. Kee, D. Bierschenk, and S. A. Barnett, *J. Power Sources*, **187**, 123 (2009).
64. V. M. Janardhanan and O. Deutschmann, *J. Power Sources*, **162**, 1192 (2006).
65. G. Franceschini and S. Macchietto, *Chem. Eng. Sci.*, **63**, 4846 (2008).
66. gPROMS (General Process Modelling and Simulation Tool), v3.2, Process Systems Enterprise Ltd., London.
67. P. Metzger, K.-A. Friedrich, H. Müller-Steinhagen, and G. Schiller, *Solid State Ionics*, **177**, 2045 (2006).
68. Z. Wuillemin, Ph.D. Thesis, Ecole Polytechnique Fédérale de Lausanne, Lausanne (2009).
69. F. Ravussin, J. Van herle, N. Autissier, M. Molinelli, D. Larrain, and D. Favrat, *J. Eur. Ceram. Soc.*, **27**, 1035 (2007).
70. A. Nakajo, P. Tanasini, J. Van herle, and D. Favrat, *J. Electrochem. Soc.*, **158**, B1102 (2011).
71. A. M. Svensson, S. Sunde, and K. Nisancioğlu, *J. Electrochem. Soc.*, **144**, 2719 (1997).
72. Z. Wuillemin, A. Nakajo, A. Müller, A. J. Schuler, S. Diethelm, J. Van herle, and D. Favrat, *ECS Trans.*, **25**(2), 457 (2009).
73. S. Diethelm, J. Van herle, Z. Wuillemin, A. Nakajo, N. Autissier, and M. Molinelli, *J. Fuel Cell Sci. Technol.*, **5**, 3 (2008).
74. D. Larrain, Ph.D. Thesis, Ecole Polytechnique Fédérale de Lausanne, Lausanne (2005).
75. F. P. Incropera, D. P. DeWitt, T. L. Bergman, and A. S. Lavine, *Fundamentals of Heat and Mass Transfer 75*: Wiley (1996).
76. C. Stiller, B. Thorud, S. Seljebø, Ø. Mathisen, H. Karoliussen, and O. Bolland, *J. Power Sources*, **141**, 227 (2005).
77. B. Todd and J. B. Young, *J. Power Sources*, **110**, 186 (2002).
78. R. Vaßen, D. Simwonis, and D. Stöver, *J. Mater. Sci.*, **36**, 147 (2001).
79. J. Kondoh, T. Kawashima, S. Kikuchi, Y. Tomii, and Y. Ito, *J. Electrochem. Soc.*, **145**, 1527 (1998).
80. J. Kondoh, S. Kikuchi, Y. Tomii, and Y. Ito, *J. Electrochem. Soc.*, **145**, 1536 (1998).
81. J. Kondoh, S. Kikuchi, Y. Tomii, and Y. Ito, *J. Electrochem. Soc.*, **145**, 1550 (1998).
82. K. Nisancioğlu, in Ohmic losses, Proceedings of the IEA Workshop on Mathematical Modelling, Charmey, International Energy Agency, p. 87 (1998).
83. J. Fleig, H. L. Tuller, and J. Maier, *Solid State Ionics*, **174**, 261 (2004).
84. A. Bieberle, L. P. Meier, and L. J. Gauckler, *J. Electrochem. Soc.*, **148**, A646 (2001).
85. J. Mizusaki, H. Tagawa, T. Saito, T. Yamamura, K. Kamitani, K. Hirano, S. Ehara, T. Takagi, T. Hikita, M. Ippommatsu, S. Nakagawa, and K. Hashimoto, *Solid State Ionics*, **70-71**, 52 (1994).
86. B. de Boer, Ph.D. Thesis, University of Twente, Enschede, The Netherlands (1998).
87. M. Vogler, A. Bieberle-Hütter, L. Gauckler, J. Warnatz, and W. G. Bessler, *J. Electrochem. Soc.*, **156**, B663 (2009).
88. A. Bieberle and L. J. Gauckler, *Solid State Ionics*, **135**, 337 (2000).
89. M. Brown, S. Primdahl, and M. Mogensen, *J. Electrochem. Soc.*, **147**, 475 (2000).
90. X. Wang, N. Nakagawa, and K. Kato, *J. Electrochem. Soc.*, **148**, A565 (2001).
91. S. Primdahl and M. Mogensen, *J. Appl. Electrochem.*, **30**, 247 (2000).
92. S. P. Jiang and Y. Ramprakash, *Solid State Ionics*, **116**, 145 (1999).
93. S. P. Jiang and Y. Ramprakash, *Solid State Ionics*, **122**, 211 (1999).
94. P. Holtappels, L. G. J. de Haart, and U. Stimming, *J. Electrochem. Soc.*, **146**, 1620 (1999).
95. P. Holtappels, I. C. Vinke, L. G. J. de Haart, and U. Stimming, *J. Electrochem. Soc.*, **146**, 2976 (1999).
96. Y. L. Liu, S. Primdahl, and M. Mogensen, *Solid State Ionics*, **161**, 1 (2003).
97. A. Bieberle and L. J. Gauckler, *Solid State Ionics*, **146**, 23 (2002).
98. H. Zhu, R. J. Kee, V. M. Janardhanan, O. Deutschmann, and D. G. Goodwin, *J. Electrochem. Soc.*, **152**, A2427 (2005).
99. G. Franceschini and S. Macchietto, *Ind. Eng. Chem. Res.*, **46**, 220 (2007).
100. R. Krishna and J. A. Wesselingh, *Chem. Eng. Sci.*, **52**, 861 (1997).
101. E. S. Hecht, G. K. Gupta, H. Zhu, A. M. Dean, R. J. Kee, L. Maier, and O. Deutschmann, *Appl. Catal., A*, **295**, 40 (2005).
102. R. Leinfelder, Ph.D. Thesis, Universität Erlangen-Nürnberg, Erlangen-Nürnberg, Germany, (2004).
103. S. B. Adler, *Chem. Rev.*, **104**, 4791 (2004).
104. T. Kawada, J. Suzuki, M. Sase, A. Kaimai, K. Yashiro, Y. Nigara, J. Mizusaki, K. Kawamura, and H. Yugami, *J. Electrochem. Soc.*, **149**, E252 (2002).
105. T. Kawada, K. Masuda, J. Suzuki, A. Kaimai, K. Kawamura, Y. Nigara, J. Mizusaki, H. Yugami, H. Arashi, N. Sakai et al., *Solid State Ionics*, **121**, 271 (1999).
106. E. Siebert, A. Hammouche, and M. Kleitz, *Electrochim. Acta*, **40**, 1741 (1995).
107. T. Horita, K. Yamaji, M. Ishikawa, N. Sakai, H. Yokokawa, T. Kawada, and T. Kato, *J. Electrochem. Soc.*, **145**, 3196 (1998).
108. F. H. van Heuveln and H. J. M. Bouwmeester, *J. Electrochem. Soc.*, **144**, 134 (1997).
109. E. P. Murray, T. Tsai, and Scott A. Barnett, *Solid State Ionics*, **110**, 235 (1998).
110. M. J. Jørgensen and M. Mogensen, *J. Electrochem. Soc.*, **148**, A433 (2001).
111. S. P. Jiang and W. Wang, *Electrochem. Solid-State Lett.*, **8**, A115 (2005).
112. M. Mosleh, M. Sogaard, and P. V. Hendriksen, *J. Electrochem. Soc.*, **156**, B441 (2009).
113. M. Sogaard, P. V. Hendriksen, and M. Mogensen, *J. Solid State Chem.*, **180**, 1489 (2007).
114. J. Mizusaki, M. Yoshihiro, S. Yamauchi, and K. Fueki, *J. Solid State Chem.*, **58**, 257 (1985).
115. J. E. ten Elshof, M. H. R. Lankhorst, and H. J. M. Bouwmeester, *J. Electrochem. Soc.*, **144**, 1060 (1997).
116. M. H. R. Lankhorst and J. E. ten Elshof, *J. Solid State Chem.*, **130**, 302 (1997).
117. H. J. M. Bouwmeester, M. W. D. Otter, and B. A. Boukamp, *J. Solid State Electrochem.*, **8**, 599 (2004).
118. J. E. ten Elshof, M. H. R. Lankhorst, and H. J. M. Bouwmeester, *Solid State Ionics*, **99**, 15 (1997).
119. D. Mantzavinos, A. Hartley, I. S. Metcalfe, and M. Sahibzada, *Solid State Ionics*, **134**, 103 (2000).
120. S. B. Adler, X. Y. Chen, and J. R. Wilson, *J. Catal.*, **245**, 91 (2007).
121. X. J. Chen, S. H. Chan, and K. A. Khor, *Electrochim. Acta*, **49**, 1851 (2004).
122. Y. Jiang, S. Wang, Y. Zhang, J. Yan, and W. Li, *Solid State Ionics*, **110**, 111 (1998).
123. J. S. Newman and K. E. Thomas-Alyea, *Electrochemical Systems*, p. 289, Wiley Interscience, New York (2004).
124. Z. Yang and Y. S. Lin, *Solid State Ionics*, **150**, 245 (2002).
125. Y. Matsuzaki and I. Yasuda, *Solid State Ionics*, **126**, 307 (1999).
126. D. Gostovic, J. R. Smith, D. P. Kundinger, K. S. Jones, and E. D. Wachsman, *Electrochem. Solid-State Lett.*, **10**, B214 (2007).
127. D. Simwonis. Optimierung der Anoden der Hochtemperatur-Brennstoffzelle durch Korrelation von Herstellungsverfahren, Gefüge und Eigenschaften; Jül-report 3678. Edited by Forschungszentrum Jülich, Germany (1999).
128. A. Hagen, Y. L. Liu, R. Barfod, and P. V. Hendriksen, *J. Electrochem. Soc.*, **155**, B1047 (2008).
129. Z. Wuillemin, N. Autissier, A. Nakajo, M.-T. Luong, J. Van herle, and D. Favrat, *J. Fuel Cell Sci. Technol.*, **5**, 011016 (2008).
130. C. M Kleinlogel and L. J. Gauckler, *J. Electrochem. Soc.*, **5**, 231 (2000).
131. S. Kuharungrong, *Ceram. Int.*, **30**, 273 (2004).
132. K. T. S. Thyden. Ph.D. Thesis, Technical University of Denmark, Risø National Laboratory for Sustainable Energy, Fuel Cells and Solid State Chemistry Division 132 (2008).